# NAVAL POSTGRADUATE SCHOOL
## Monterey, California


FY 73 HYDRAULIC RAM STUDIES

A. E. Fuhs, R. E. Ball, & H. L. Power

February 1974

Final Report for Period 1 July 1972-30 June 1973



Prepared for:
Naval Weapons Center
China Lake, California 93555
and
Air Force Flight Dynamics Laboratory
Wright-Patterson AFB, Ohio 45433

NAVAL POSTGRADUATE SCHOOL
Monterey, California

Rear Admiral Mason Freeman
Superintendent

Jack R. Borsting
Provost

The work reported herein was supported by the Naval Weapons Center, China Lake, California and the Air Force Flight Dynamics Laboratory, Wright-Patterson AFB, Ohio.



This report was prepared by:

UNCLASSIFIED

SECURITY CLASSIFICATION OF THIS PAGE *(When Date Entered)*

| REPORT DOCUMENTATION PAGE | | READ INSTRUCTIONS BEFORE COMPLETING FORM |
|---|---|---|
| 1. REPORT NUMBER<br>NPS-57Fu74021 | 2. GOVT ACCESSION NO. | 3. RECIPIENT'S CATALOG NUMBER |
| 4. TITLE *(and Subtitle)*<br>FY 73 Hydraulic Ram Studies | | 5. TYPE OF REPORT & PERIOD COVERED<br>Final Report<br>1 July 1972 - 30 June 1973 |
| | | 6. PERFORMING ORG. REPORT NUMBER |
| 7. AUTHOR*(s)*<br>A. E. Fuhs, R. E. Ball & H. L. Power | | 8. CONTRACT OR GRANT NUMBER*(s)* |
| 9. PERFORMING ORGANIZATION NAME AND ADDRESS<br>Naval Postgraduate School<br>Monterey, California 93940 | | 10. PROGRAM ELEMENT, PROJECT, TASK AREA & WORK UNIT NUMBERS<br>PO-3-0080, 21 Dec. 1972<br>MIPP #FY1456-74-0001, June 73 |
| 11. CONTROLLING OFFICE NAME AND ADDRESS<br>Naval Weapons Center, China Lake, Calif. 93555<br>and Air Force Flight Dynamics Laboratory,<br>Wright-Patterson AFB, Ohio 45433 | | 12. REPORT DATE<br>February 1, 1974 |
| | | 13. NUMBER OF PAGES<br>79 |
| 14. MONITORING AGENCY NAME & ADDRESS*(if different from Controlling Office)* | | 15. SECURITY CLASS. *(of this report)*<br>Unclassified |
| | | 15a. DECLASSIFICATION/DOWNGRADING SCHEDULE |

16. DISTRIBUTION STATEMENT *(of this Report)*

Approved for public release; distribution unlimited.

17. DISTRIBUTION STATEMENT *(of the abstract entered in Block 20, if different from Report)*

18. SUPPLEMENTARY NOTES

19. KEY WORDS *(Continue on reverse side if necessary and identify by block number)*

Aircraft Survivability
Aircraft Vulnerability
Fuel Cells
Hydraulic Ram

20. ABSTRACT *(Continue on reverse side if necessary and identify by block number)*

This document is a report on the progress of FY 73 Hydraulic Ram studies. Preliminary analytical and experimental studies of the shock and cavity phases of hydraulic ram have been made to add to basic understanding of the fluid-structural interactions. This work should contribute to the understanding of the hydraulic ram phenomenon and will provide useful information when designing survivable fuel tanks in aircraft.

DD FORM 1 JAN 73 1473 EDITION OF 1 NOV 65 IS OBSOLETE
S/N 0102-014-6601 |
(Page 1)

UNCLASSIFIED

SECURITY CLASSIFICATION OF THIS PAGE *(When Date Entered)*

TABLE OF CONTENTS


| Section | | Page |
|---|---|---|
| I. | INTRODUCTION | 2 |
| II. | ANALYTICAL AND NUMERICAL STUDIES | 4 |
| | A. A STUDY OF WALL MOTION | 4 |
| | B. ENTRY WALL RESPONSE TO THE SHOCK PHASE | 16 |
| | C. MODIFICATION OF NORTHROP INTERNAL BLAST CODE | 22 |
| | D. ANALYSIS OF CAVITY MOTION | 25 |
| III. | HYDRAULIC RAM EXPERIMENTAL FACILITIES | 31 |
| | A. INTRODUCTION | 31 |
| | B. BALLISTIC RANGE COMPONENTS | 32 |
| | C. EXPERIMENTAL | 42 |
| IV. | TEST RESULTS TO DATE | 46 |
| | A. PENETRATION STUDIES | 46 |
| | B. SHOCK PHASE STUDIES | 54 |
| | 1. SHADOWGRAPHS OF FUEL TANK FLOW FIELD | 54 |
| | 2. DEFORMATION OF LEAD PROJECTILES | 58 |
| V. | RECOMMENDATIONS FOR FURTHER STUDY | 74 |
| VI. | CITED REFERENCES | 75 |
| VII. | LIST OF FIGURES | 76 |

# I. INTRODUCTION

Fuel tanks comprise the greatest portion of vulnerable target volume in modern military aircraft. This degree of vulnerability of the fuel tanks is of paramount importance in determining aircraft survivability. Fuel tanks which are subjected to ballistic impact can sustain severe damage as a result of the phenomenon known as hydraulic ram. For our purposes, hydraulic ram is defined as the production of pressure loadings by ballistic impact and their effects on the fuel tank and its components. The term hydraulic ram is a misnomer in that it suggests a quasi-static compression process. Actually the mechanism of hydraulic ram consists of several phases. The shock phase is generated when the projectile penetrates the tank wall. Projectile penetration produces a stress riser in the tank wall from which cracks can propagate radially. Shock wave formation in the fuel due to projectile penetration into the fluid causes very high local pressures which may be sufficient to cause failure of the entry wall in the neighborhood of the entry point. As the projectile moves through the fluid it leaves a vapor-filled void caused by flow separation from the projectile surface. During this so-called cavity phase the projectile's kinetic energy is transferred to the fluid by cavity formation. Cavity growth is subsequently defeated by hydrostatic pressure and the cavity collapses. The collapse is not total because of fluid vapor compression. The cavity oscillates until equilibrium is reached in the fluid. Cavity oscillations produce corresponding pressure loadings on the tank walls which can cause catastropic failure of tank components. The exit wall of the tank is also heavily loaded as the projectile passes through.

The purpose of the investigation to date has been to develop an

understanding of the hydraulic ram phenomenon. Fuel tank response to ballistic penetration cannot be fully understood without comprehension of the individual hydraulic ram components and their interaction. This understanding can be obtained by conducting experiments and developing analytical-numerical tools which predict the events that occur during the damaging processes. With this understanding and the analytical-numerical tools available, fuel tanks which minimize hydraulic ram can be designed. Once fuel tanks are protected against this type of threat, aircraft vulnerability will be lessened.

## II. ANALYTICAL AND NUMERICAL STUDIES

### A. A Study of the Wall Motion, Treated as a Single Degree of Freedom System (Development of Piston Theory)

Consider a typical portion of a fuel tank wall treated as a single degree of freedom system as shown in Fig. II-A-1. The area of the portion of the wall is A and the total mass is M. The resistance to displacement provided by the surrounding wall is modeled by the spring, whose constant is K. The equation governing the elastic motion of the wall is assumed to be

$$M\ddot{w} + Kw = Ap(t) \qquad \text{(II-A-1)}$$

where p(t) is the total time dependent pressure on the wall due to the incident pressure waves in the fluid and to the waves reflected and radiated from the wall and w is the wall displacement. The dots indicate derivatives with respect to time t. Assuming that the fluid satisfies the linear wave equation and applying a step pressure pulse normal to the wall as the incident wave gives

$$p(t) = 0 \qquad t < 0$$

$$p(t) = p_o - \rho\dot{\phi}_i \qquad t \geq 0 \qquad \text{(II-A-2)}$$

where $p_o$ is the pressure in the incident wave, $\rho$ is the fluid density, and $\phi$ is the velocity potential of the reflected and radiated waves. The subscript i denotes the value of $\phi$ at the wall. The potential $\phi$ is governed by the wave equation

$$c^2\phi'' = \ddot{\phi} \qquad \text{(II-A-3)}$$

where c is the acoustic velocity in the fluid and primes denote derivatives with respect to x, the axial space coordinate normal to the wall. At the wall the velocity of the fluid is equal to the velocity of the wall. Thus,

$$\dot{w} = v_i + \phi_i' \qquad \text{(II-A-4)}$$

where $v_i$ is the velocity of the incident wave and is equal to $p_o/(\rho c)$.

Equations (1), (2), (3), and (4) govern the behavior of the fluid-structure interaction process. The solution to Equation (3) for $\phi$ can be given in the form

$$\phi = \alpha e^{i\lambda(x+ct)/a} + \beta e^{i\lambda(x-ct)/a} \qquad \text{(II-A-5)}$$

where $\alpha$ and $\beta$ are arbitrary constants, $\lambda$ is a scalar, and a is the value of x at the wall. The first quantity on the r.h.s. of Equation (5) represents waves traveling away from the wall, and the second quantity represents waves traveling toward the wall. Note that for the waves traveling away from the wall, i.e., the reflected and radiated waves,

$$\dot{\phi} = c\phi' \qquad \text{(II-A-6)}$$

Thus,

$$\dot{w} = v_i + \frac{1}{c}\dot{\phi}$$

according to Equation (4). Hence

$$\dot{\phi} = c(\dot{w} - v_i) \qquad \text{(II-A-7)}$$

Substituting $\dot{\phi}$ given by Equation (7) into Equation (2) gives

$$p(t) = p_o + \rho c(v_i - \dot{w}) \qquad t \geq 0 \tag{II-A-8}$$

Examination of Equations (1) and (8) reveals that the variables $\phi$ and w have now been separated, i.e., the response of the wall can be computed based upon the pressure and velocity of the incident pressure wave. Application of Equation (8) to the more general two-dimensional wall response is known as the piston theory (Refs. 1 and 2). Substituting Equation (8) into Equation (1) leads to

$$\ddot{w} + 2\zeta\omega\dot{w} + \omega^2 w = \frac{\bar{p}_o}{m} \tag{II-A-9}$$

where

$$\omega^2 = \frac{K}{M}$$

$$\zeta = \frac{\rho c}{2m\omega}$$

$$\bar{p}_o = p_o + \rho c v_i = 2p_o$$

$$m = \frac{M}{A}$$

The solution to Equation (9) can be given in the form

$$w = w_{st}\left\{1 - e^{-\zeta\omega t}\left[\frac{\zeta+\sqrt{\zeta^2-1}}{2\sqrt{\zeta^2-1}}\, e^{\omega\sqrt{\zeta^2-1}\, t} - \frac{\zeta-\sqrt{\zeta^2-1}}{2\sqrt{\zeta^2-1}}\, e^{-\omega\sqrt{\zeta^2-1}\, t}\right]\right\} \tag{II-A-10a}$$

$$\dot{w} = w_{st}\frac{\omega}{2\sqrt{\zeta^2-1}}\, e^{-\zeta\omega t}\left(e^{\omega\sqrt{\zeta^2-1}\, t} - e^{-\omega\sqrt{\zeta^2-1}\, t}\right) \tag{II-A-10b}$$

$$p = \bar{p}_o \left\{ 1 - \frac{\zeta}{\sqrt{\zeta^2-1}} \; e^{-\zeta\omega t} \left[ e^{\omega\sqrt{\zeta^2-1}\; t} - e^{-\omega\sqrt{\zeta^2-1}\; t} \right] \right\} \qquad \text{(II-A-10c)}$$

where

$$w_{st} = \frac{A\bar{p}_o}{K} = \frac{\bar{p}_o}{m\omega^2}$$

when the wall is at rest prior to the application of the step pressure.

If the contribution of the spring is neglected, we have a one-dimensional pressure wave reflecting off of an infinite wall. Hence, $\omega = 0$, $\zeta = \infty$, $\zeta\omega = \frac{1}{2}\frac{\rho c}{m}$ . This problem was considered in Ref. 3, where the equation for the pressure on the wall was taken as

$$p(t) = p_o \, e^{-\frac{\rho c t}{m}} \qquad \text{(II-A-10d)}$$

Typical values for c, $\rho$ and m for hydraulic ram in fuel tanks are

$$c = 53{,}600 \text{ in./sec}$$

$$\rho = 7.64 \times 10^{-5} \text{ \#-sec}^2/\text{in.}^4$$

$$m = 2.59 \times 10^{-5} \text{ \#sec}^2/\text{in.}^3 \quad \text{(0.1 in. aluminum wall)}$$

$$= 3.64 \times 10^{-4} \text{ \#sec}^2/\text{in.}^3 \quad \text{(0.5 in. steel wall)}$$

Therefore

$$\frac{\rho c}{m} = 0.158 \times 10^6 \frac{1}{\text{sec}} \quad \text{(0.1 in. aluminum wall)}$$

$$\frac{\rho c}{m} = 0.01125 \times 10^6 \frac{1}{\text{sec}} \quad \text{(0.5 in. steel wall)}$$

Consequently, when $\omega < 15000$ rad/sec for the 0.1 in. aluminum wall and $\omega < 1000$ rad/sec for the 0.5 in. steel wall, $\zeta >> 1$, i.e., the

system is heavily damped, and Equations (10a - 10c) simplify to

$$w = w_{st}\left\{1 - e^{-\frac{\omega t}{2\zeta}} - \frac{1}{4\zeta^2}\left(e^{-\frac{\omega t}{2\zeta}} - e^{\frac{\omega t}{2\zeta}}\, e^{-2\zeta\omega t}\right)\right\} \qquad \text{(II-A-11a)}$$

$$\dot{w} = w_{st}\left(\frac{\omega}{2\zeta}\right)\left(e^{-\frac{\omega t}{2\zeta}} - e^{\frac{\omega t}{2\zeta}}\, e^{-2\zeta\omega t}\right) \qquad \text{(II-A-11b)}$$

$$p = \bar{p}_o\left(1 - e^{-\frac{\omega t}{2\zeta}} + e^{\frac{\omega t}{2\zeta}}\, e^{-2\zeta\omega t}\right) \qquad \text{(II-A-11c)}$$

A plot of $\frac{p}{p_o}$ versus time is given in Fig. II-A-2a for $\frac{\rho c}{m}$ = 0.2, 0.1, 0.05, and 0.01 x $10^6$ $\frac{1}{\text{sec}}$, and 1 μsec. In this figure the assumption is made that $\frac{m\omega^2}{\rho c} < 100$, i.e., $\omega < 1{,}000$ rad/sec for $\frac{\rho c}{m}$ = 0.01 x $10^6$ $\frac{1}{\text{sec}}$ and $\omega < 4{,}470$ for $\frac{\rho c}{m}$ = 0.2 x $10^6$ $\frac{1}{\text{sec}}$. Under these conditions, Equation (11c) for p simplifies to Equation (10d), provided $t < 500$ μsec. Curves of this type are also given in Ref. 3, Fig. 8, for a 1 inch plexiglas wall and a 0.063 inch aluminum wall with an exponentially decaying incident pressure wave.

For $t > 500$ μsec the elastic property of the wall begins to become effective and reduces the wall velocity. This causes the pressure to build up. A plot of $\frac{p}{\bar{p}_o}$ is given in Fig. II-A-2b for $\frac{m\omega^2}{\rho c}$ = 100, 20, 10 and 5 $\frac{1}{\text{sec}}$, and 100 μsec $\leq t \leq$ 100,000 μsec. For these conditions, Equations (11a - 11c) simplify to

$$w = w_{st}\left(1 - e^{-\frac{\omega t}{2\zeta}}\right)\ ,\quad \dot{w} = w_{st}\left(\frac{\omega}{2\zeta}\right)e^{-\frac{\omega t}{2\zeta}}\ ,\quad p = \bar{p}_o\left(1 - e^{\frac{\omega t}{2\zeta}}\, e^{-2\rho\omega t}\right) \qquad \text{(II-A-12)}$$

Examination of Figs. II-A-2a and 2b reveals that for the values of the parameters considered, the inertial effects and the elastic effects occur in essentially separate periods of time. This is due to the

assumption on $\omega$. When the stress wave strikes the wall, the wall deflects as if there were no elastic effects. After approximately 500-1000 $\mu$sec the wall starts to slow down due to the elastic effects, the pressure builds up, and eventually the wall comes to rest. The motion of the wall is that of a heavily damped oscillator*. This phenomenon holds provided

$$\frac{m\omega^2}{m} < 100 \frac{1}{sec}$$

For

$$\frac{\rho c}{m} = 0.01 \times 10^6 \frac{1}{sec} \quad , \quad \omega < 1000 \text{ rad/sec}$$

The lowest natural frequency of a square plate of width L is

$$\omega = \frac{2\pi^2}{L^2} \sqrt{\frac{Eh^2}{12(1-\upsilon^2)\rho}} \qquad \text{(II-A-13)}$$

where E is Young's modulus, h is the wall thickness, and $\upsilon$ is Poisson's ratio. For both aluminum and steel walls

$$\omega \approx 1.2 \times 10^5 \left(\frac{h}{L^2}\right) \text{ rad/sec} \qquad \text{(II-A-14)}$$

For

L = 20 in. and h = 0.5 in. , $\omega \approx 150$ rad/sec

For

L = 10 in. and h = 0.5 in. , $\omega \approx 600$ rad/sec

---

*The natural frequency for critical damping is 79,000 rad/sec (12,600 Hz) for the 0.1 aluminum wall, and is 5,620 rad/sec (884 Hz) for the 0.5 in. steel wall.

Thus, $\omega < 1000$ rad/sec is a realistic limit for the fundamental frequency of fuel tank walls.

Since the elastic response takes place relatively late in the interaction process, the question arises as to the possible validity of treating the stress wave as an impulse loading. For example, suppose the incident pressure pulse at the wall is of the type shown below

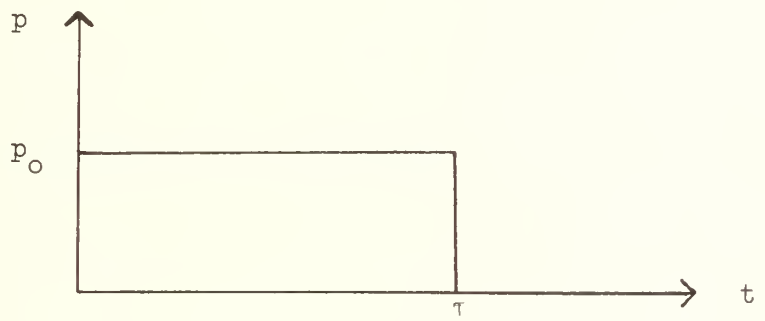


The solution for the wall displacement (provided $\zeta > 1$) for $t > \tau$ is

$$w = \left[ w_\tau \left( 1 + \frac{1}{4\zeta^2} \right) + \frac{\dot{w}_\tau}{2\zeta\omega} \right] e^{-\frac{(t-\tau)\omega}{2\zeta}} - \left[ \frac{w_\tau}{4\zeta^2} + \frac{\dot{w}_\tau}{2\zeta\omega} \right] e^{\frac{\omega(t-\tau)}{2\zeta}} e^{-2\zeta\omega(t-\tau)} \qquad \text{(II-A-15)}$$

$$t \geq \tau$$

where $w_\tau$ and $\dot{w}_\tau$ are the displacement and velocity of the wall at $t = \tau$. The first term in Equation (15) is the long time response; the second term damps out very quickly. If the stress wave pulse is treated as an impulsive loading, the displacement and velocity at $t = \tau$ are

$$w_\tau = 0$$

$$\dot{w}_\tau = \frac{\bar{p}_o}{m} \tau$$

Hence

$$w_{impulse} = \frac{\bar{p}_o \tau}{2\zeta\omega m} \left( e^{-\frac{\omega(t-\tau)}{2\zeta}} - e^{\frac{\omega(t-\tau)}{2\zeta}} e^{-2\zeta\omega(t-\tau)} \right) \qquad \text{(II-A-16)}$$

The correct solution for w using Equations (10a) and (10b) to define $w_\tau$ and $\dot{w}_\tau$ is

$$w_\tau = \frac{\bar{p}_o}{m\omega^2}\left(1-e^{-\frac{\omega\tau}{2\zeta}}\right) - \frac{\dot{w}_\tau}{2\zeta\omega}$$

$$\dot{w}_\tau = \frac{\bar{p}_o}{2\zeta\omega m}\left(e^{-\frac{\omega\tau}{2\zeta}} - e^{\frac{\omega\tau}{2\zeta}} e^{-2\zeta\omega\tau}\right)$$

and

$$w \approx \frac{\bar{p}_o}{m\omega^2}\left\{\left(1-e^{-\frac{\omega\tau}{2\zeta}}\right)e^{-\frac{\omega(t-\tau)}{2\zeta}} - \frac{1}{4\zeta^2}\left(1-e^{\frac{\omega\tau}{2\zeta}} e^{-2\zeta\omega\tau}\right) e^{\frac{\omega(t-\tau)}{2\zeta}} e^{-2\zeta\omega(t-\tau)}\right\} \qquad \text{(II-A-17)}$$

$$t \geq \tau$$

provided $\zeta >> 1$. When $\tau$ is such that

$$e^{-\frac{\omega\tau}{2\zeta}} \approx 1 - \frac{\omega\tau}{2\zeta}$$

i.e., $\tau << \frac{\rho c}{m\omega^2}$, Equation (17) simplifies to

$$w \approx \frac{\bar{p}_o}{2\zeta\omega m}\left(e^{-\frac{\omega(t-\tau)}{2\zeta}} + \frac{1}{4\zeta^2} e^{-2\zeta\omega\tau} e^{\frac{\omega(t-\tau)}{2\zeta}} e^{-2\zeta\omega(t-\tau)}\right) \quad , \quad t \geq \tau \qquad \text{(II-A-18)}$$

Thus, comparing Equations (16) and (18) reveals that the long time response is correctly approximated by the impulse assumption, but the short time response is inaccurate.

The conclusions that can be drawn from this analysis are:

1. The wall responds to the pressure wave as a very heavily damped oscillator provided the natural frequency of the wall is less than 1000 rad/sec ($\approx$150 Hz).

2. The pressure on the wall drops off to a small percentage of the incident pressure within the first 100 μsec. It begins to build up when $t > 1000$ μsec. Thus, the reflected pressure from the wall is essentially the same as the reflected pressure from a free surface for the period 100 μsec $< t <$ 1000 μsec.

3. If the incident pressure is on for a finite length of time $\tau$ such that $\tau << \frac{m}{\rho c}$ $\left(\frac{\rho c}{m} = 0.158 \times 10^6 \frac{1}{\text{sec}}\right.$ for a 0.1 in. aluminum wall, $\frac{\rho c}{m} = 0.01125 \times 10^6 \frac{1}{\text{sec}}$ for a 0.5 in. steel wall$\left.\right)$ the long time response is accurately predicted but the short time response is inaccurate.

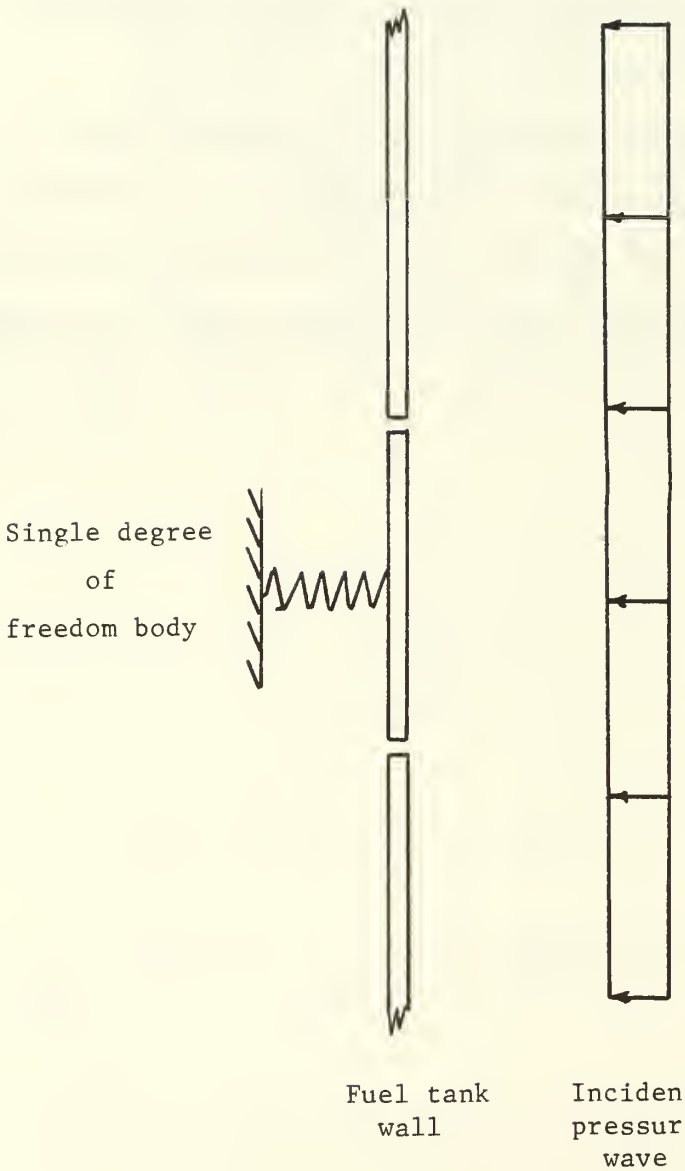


Figure II-A-1 Idealization for Single Degree of Freedom Analysis

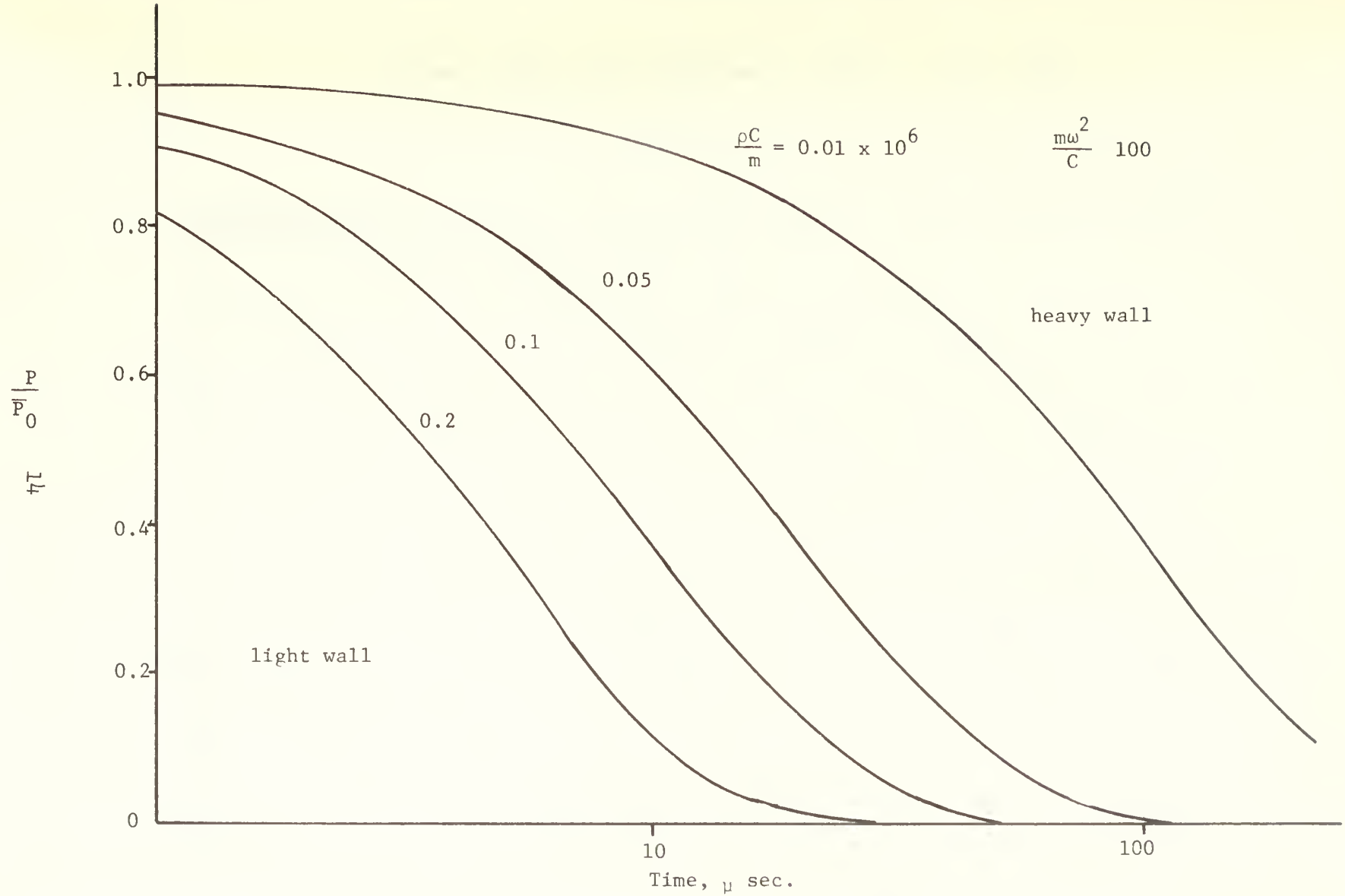


Figure II-A-2a Wall Pressure Vs. Time ($\tau$ < 1000 sec.)

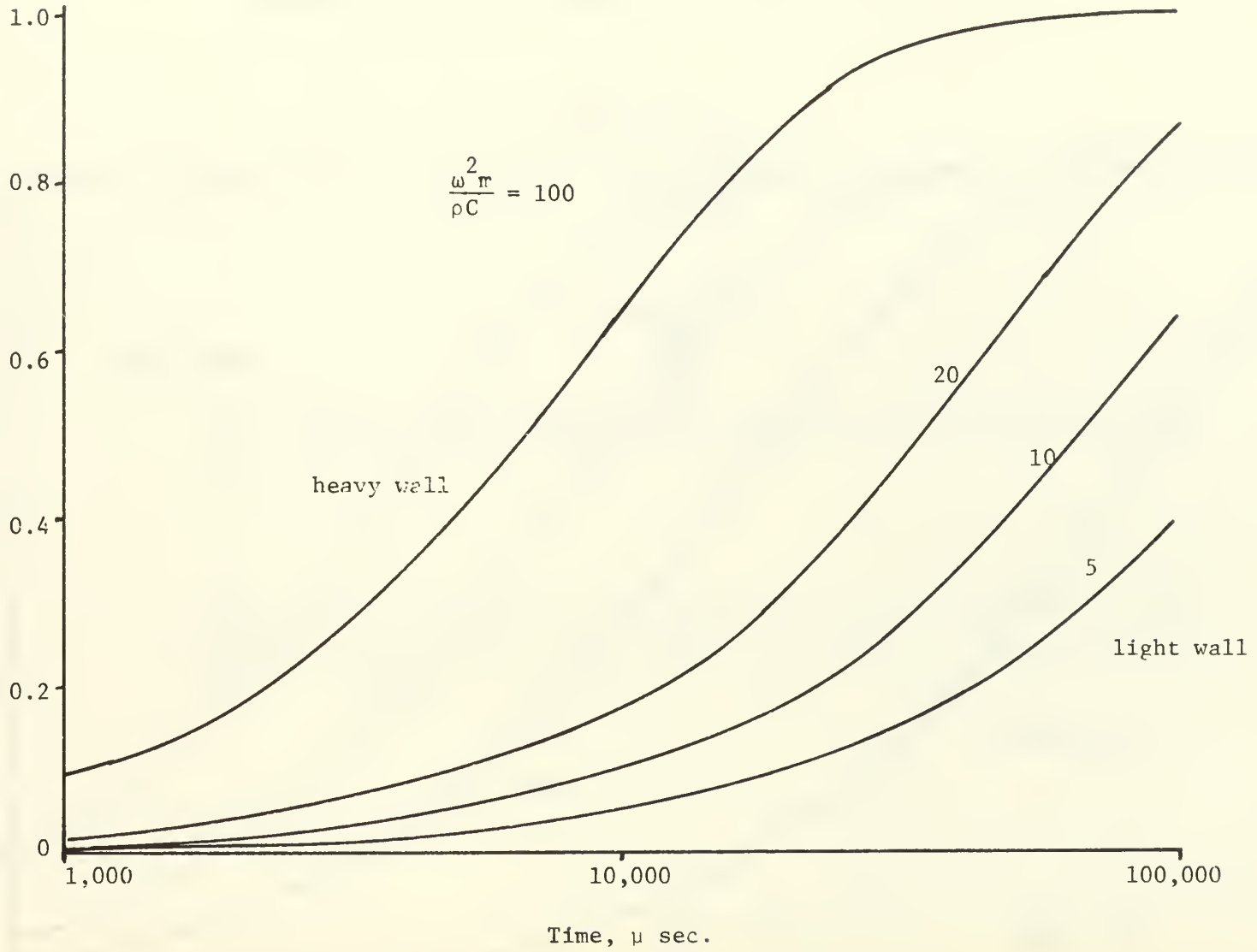


$\frac{P}{P_0}$



Figure II-A-2b Wall Pressure Vs. Time ($\tau$ > 100 μ sec.)

B. Entry Wall Response to the Shock Phase

A preliminary study of the structural response of the entrance wall of a fuel tank during the initial shock phase of the hydraulic ram has been conducted. The solution for the pressure in the fluid derived by Yurkovitch (Ref. 4) was reduced to a simple analytical form for use in the structural analysis digital computer program SATANS*. The form selected for the pressure p at a radius r and time t was

$$p(r,t) = p^* C_1^{\left(\frac{m+q-1}{1}\right)} \left(\frac{r}{C_2}\right)\left(\frac{t_1}{t}\right) \qquad 0 < t \leq t_1 C_1^{-\frac{1}{n}} \tag{II-B-1a}$$

$$p(r,t) = p^* \left(\frac{t}{t_1}\right)^{-m} \left\{1 - C_1 \left(\frac{t}{t_2}\right)^n \quad 1 - \left[\frac{r}{C_2\left(\frac{t}{t_3}\right)^q}\right]\right\}, \quad t_1 C_1^{-\frac{1}{n}} \leq t \leq \infty \tag{II-B-1b}$$

where $1 \geq \{\ \} \geq 0$. This form corresponds to a peak pressure that varies as $p^* \left(\frac{t}{t_1}\right)^{-m}$ with a linear decay behind the front to zero pressure. The location of the front is given by $C_2 \left(\frac{t}{t_3}\right)^q$. For a 0.50 caliber projectile impacting $H_2O$ (Fig. 22 of Yurkovich's report)

$$p^* = 150 \text{ ksi}$$

$$t_1 = t_2 = t_3 = 10 \ \mu\text{sec}$$

$$C_1 = 1.22$$

$$C_2 = 1.7 \text{ in.}$$

$$m = 1.2$$

*SATANS computes the transient, geometrically nonlinear response of elastic, axisymmetric plates and shells subjected to arbitrary loads. It is described in detail in Refs. 5 and 6.

$$n = 0.87$$

$$q = 0.68$$

The pressure loading given by this model is shown in Figure II-B-1 and was applied to a circular aluminum plate with a radius of 10 in. and a thickness of 0.1 in. The outer edge of the plate was assumed to be clamped. The results for the plate displacements computed by SATANS are shown in Fig. II-B-2 for t = 5, 10, 20, 30, and 50 μsec. The maximum membrane force in the plate was approximately 60,000 lb/in. and occurred at the center of the plate at $t \approx 35$ μsec. The maximum stress caused by the force and by the bending moment was 600,000 psi and 720,000 psi respectively.

The analysis for the response of the entrance wall during the shock phase discussed above neglects several important features. First, it does not take into consideration the fact that the motion of the wall relieves, to some extent, the pressure acting on the wall. Second, the very large stresses developed in the wall are considerably higher than the yield stress and the rupture stress of aluminum. Hence, yielding and cracking will occur. Third, the effects of shear deformations and rotary inertia have not been considered. Of these three features, the effect of wall motion upon the loading pressure is considered to be of prime importance in the initial phase of this program.

An exact method for determining the total fluid pressure within a closed, flexible tank has been developed by Lundstrom (Ref. 6). This model was considered as the algorithm for the pressure loading. However, due to difficulties encountered in the programming of the model, Lunstrom recommended that the piston theory be used in place of his exact model. Piston theory is described in II-A. Application of this theory uncouples the structure and fluid equations and allows

the damped response of the wall to be computed using the incident pressure as the load on the wall. This approximation has been in use since the early 1940's when it was applied to the study of the effect of underwater explosions on ship's plates.

The theory is based upon the assumption that the normal pressure on the wall is given by Equation II-A-8, i.e.,

$$p(t) = p_o + \rho_c (v_i - \dot{w})$$

which is the equation for one-dimensional fluid flow. Since SATANS did not contain the damping term $\rho c\dot{w}$, it was necessary to modify the code to incorporate this procedure.

The results for the response of the same circular plate subjected to the same pressure pulse described above but now with piston theory added, are presented in Fig. II-B-3 at several times. Comparing the two figures, II-B-2 and 3, reveals that accounting for fluid-wall interaction has a considerable effect on the wall response. Nevertheless, for this example the wall stresses are still above the yield, i.e., the maximum membrane force is 8,900 lb/in. and occurs at the center at $t = 15$ μsec, the maximum bending moment is 478 in.-lb/in. and occurs at $r = 1$ in. at $t = 15$ μsec, the maximum stress is 327 ksi and occurs at $r = 1$ in. at $t = 15$ μsec.

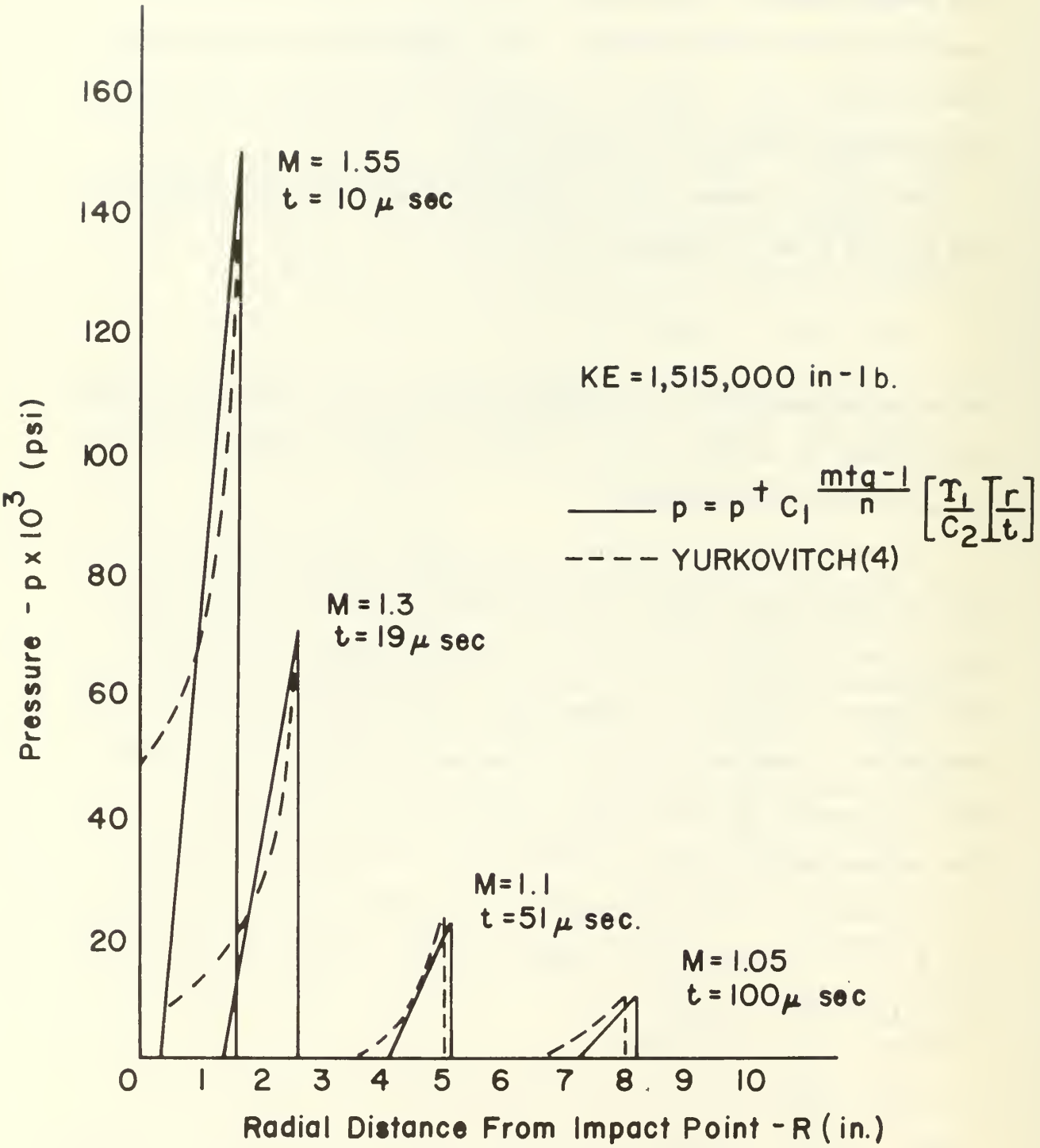


FIGURE II-B-1 SHOCK PRESSURE DISTRIBUTION FOR .50 CALIBER PROJECTILE IMPACTING $H_2O$

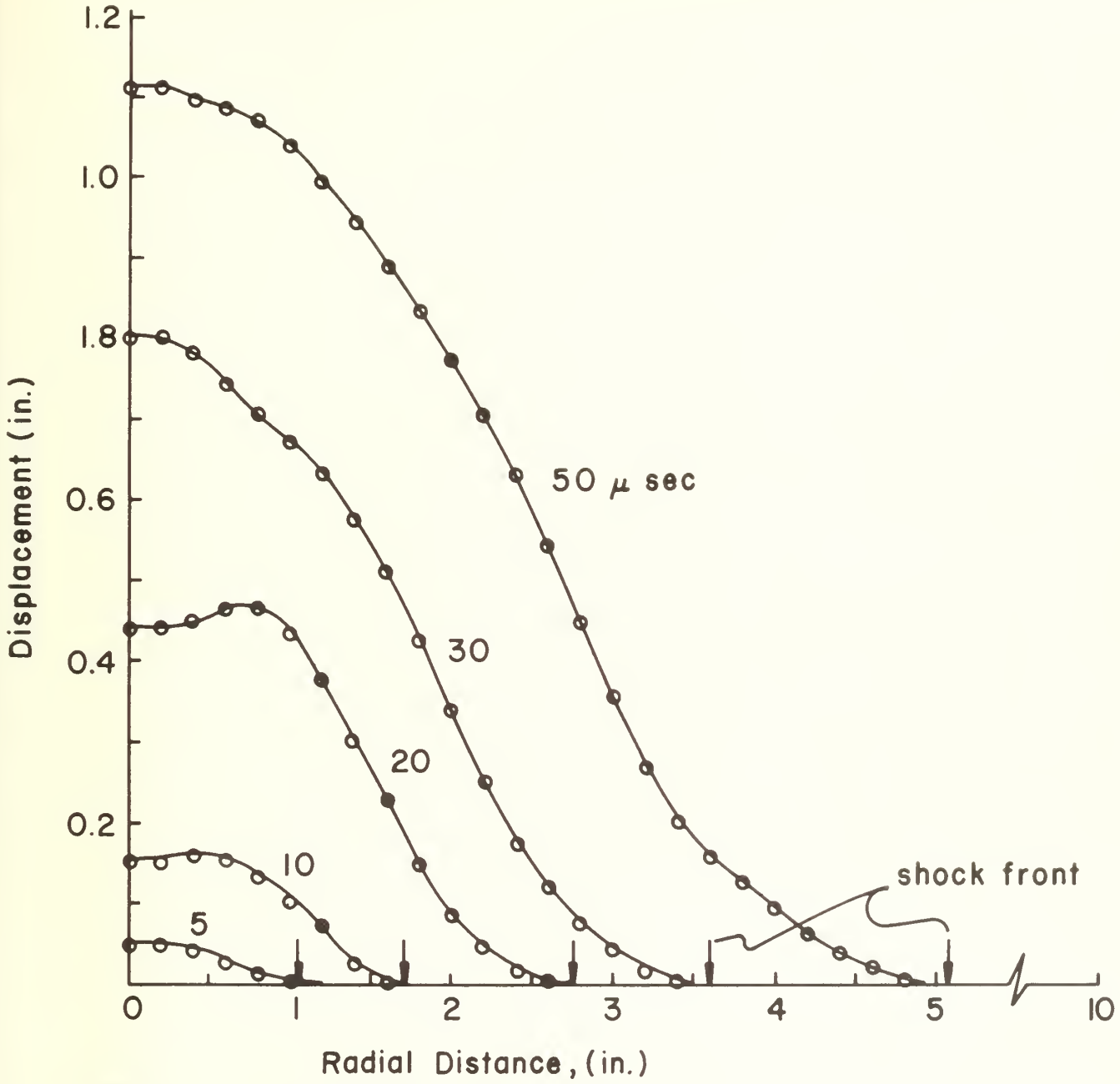


FIGURE II-B-2 NORMAL DISPLACEMENT vs. RADIAL DISTANCE WITHOUT FLUID INTERACTION

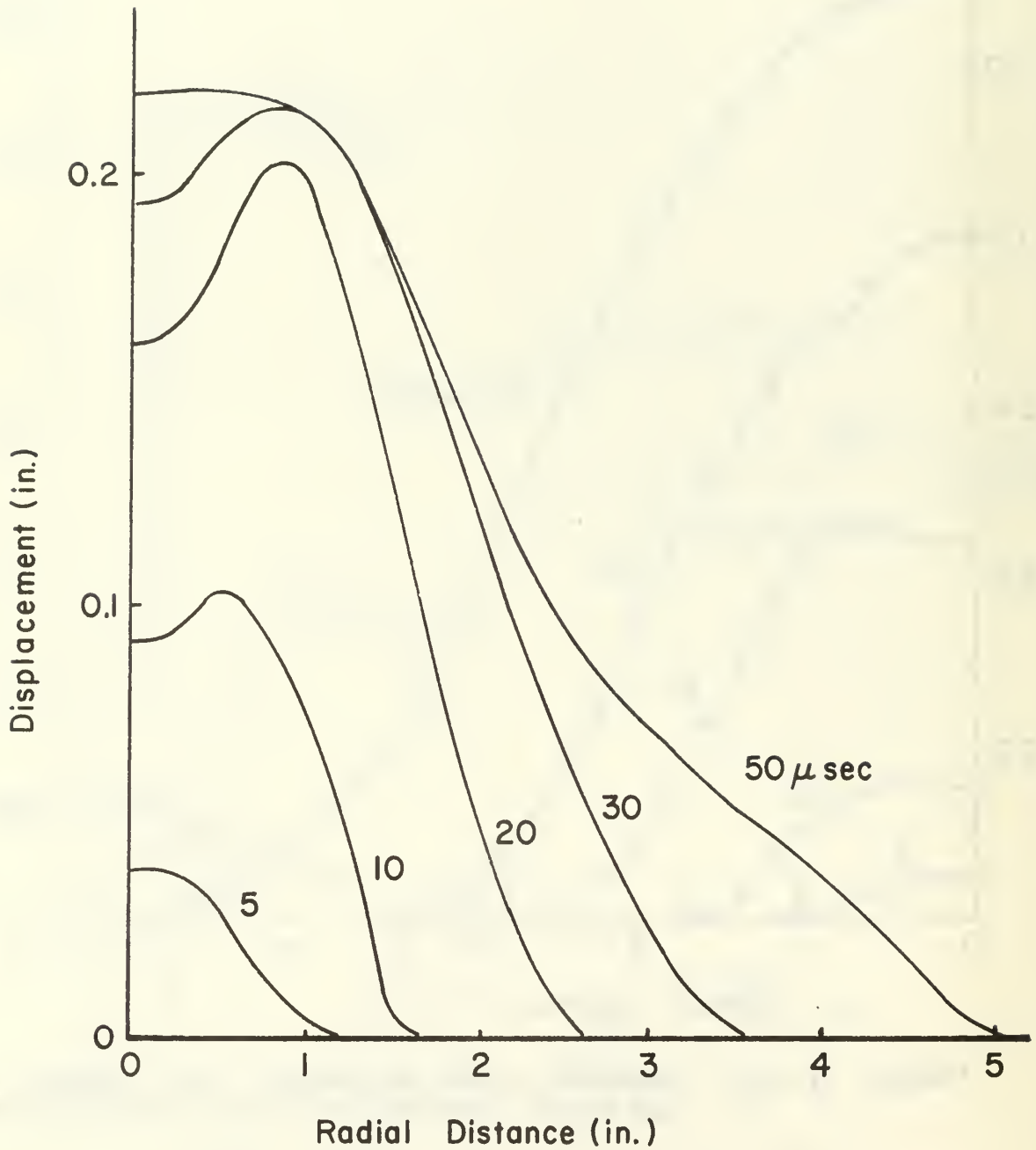


FIGURE II-B-3 DISPLACEMENT OF FUEL TANK WALL, WITH PISTON THEORY

C. Modification of the Northrop Internal Blast Code (BR-1) to Account for Hydraulic Ram Loading and Fluid-Structure Interaction

The Northrop Corporation is developing a finite element digital computer code for predicting the transient, inelastic, large deflection response of flight vehicle structures subjected to internal blast loading and fragment penetration. Ball has been following the development of this code with the objective of modifying it to account for the hydraulic ram loading and fluid-structure interaction that occurs when bullets and metal fragments penetrate aircraft fuel tank walls. The main features of the program are summarized below:

1. The elements are the isotropic flat rectangular plate and the straight beam. The cross-section of the beam element is either rectangular, I, or T-shaped.

2. The Bemoulli-Euler hypothesis is used for both the plate and the beam element.

3. The nodes of the plate element are at the four corners. The degrees of freedom at each node are the three displacements u, v, and w and two rotations $\theta_x$ and $\theta_y$. A linear edge displacement state is assumed for the inplane displacements u and v, and a cubic function is assumed for the normal displacement w.

4. Large deflection strain-displacement relationships are used for the plate element that are valid for strains as large as 10% and rotations as large as $20^{\circ}$.

5. Gaussian quadrature is used for the integration process. Three points in each direction are used.

6. The displacement state assumed for the beam element leads to an axial force, two transverse shearing forces, and a uniform torsion over the length of the element.

7. Warping of the beam due to torsion is neglected.

8. The constituitive relations for the plate and beam material incorporate the von Mises yield condition, the Prandtl-Reuss flow rule and isotropic work hardening. The material behavior is specified by a piecewise linear uniaxial stress-strain relationship. The plate cross-section is divided into four layers for the stress computations.

9. Offset points are used to relate beam element nodal to plate element nodal deflections.

10. An initial state of stress feature is available wherein each element will be in a uniform state of stress with all deflections zero.

11. Permissible loadings are distributed (pressure) loading normal to the deformed structure, either continuous or impulsive, impulsive concentrated forces at the node points, and an automated pressure fragmentation impulse loading from the NOL BLAST Code.

12. Account is taken of randomly located small perforations of a plate element due to fragment penetration by reducing the membrane and bending stiffnesses, the pressure load, and the mass.

13. The timewise numerical integration scheme is an explicit procedure.

14. The lumped mass technique is used to develop the mass matrix. Rotary inertia is considered.

15. An eigenvalue routine is incorporated to automatically determine the numerically stable time increment.

16. The program has a restart capability.

17. The code is operational on the CDC 6600 (FORTRAN EXTENDED) system. A structure with a maximum of 300 joints and 400 members can be analyzed. A total core storage of 225,000 words OCTAL (CDC system) or 270,000 bytes (IBM 320-165 system) is required.

The modifications to the BR-1 Code to make it applicable to bullet and fragment penetration into fuel tanks can be divided into two main categories: (1) incorporation of the hydraulic ram pressure loading, and (2) accounting for the fluid-structure interaction phenomena. Due to the difficulties involved in treating the fully coupled problem, the fluid-structure interaction phenomena will be approximated by the piston theory described in II-A. Thus, since the BR-1 Code does not account for damping, it will be necessary to modify the code by adding the damping term $\rho c \dot{w}$ to the equations of motion.

In the piston theory, the pressure on the structure is $p_o + \rho c v_i$ where $p_o$ is the pressure in the incident wave, $\rho$ is the fluid density, c is the acoustic velocity in the fluid, and $v_i$ is the fluid velocity. Lundstrom has developed a computer code that will predict the pressure and velocity throughout a rectangular volume of an irrotational, ideal compressible fluid due to a penetrating bullet. The boundaries of the fluid may be either free or rigid. This code will be used to determine the pressure on the fuel tank as input data to the BR-1 code.

D. Analysis of Cavity Motion

In order to gain insight to forces and velocities associated with cavity motion two problems were formulated and solved by Holm (Ref. 7). One was the collapse of a spherical cavity, an event which occurs when a vacuum exists in the cavity. The other was the oscillation of a spherical cavity with entrapped gases.

Cavity Collapse

The equations of motion for an incompressible fluid or density $\rho$ can be manipulated into the form

$$\dot{R}^2 = \frac{2}{R^3}\int_{R_o}^{R}\left(\frac{p}{\rho} - \frac{p_\infty}{\rho}\right) R^2 d\,R \qquad \text{(II-D-1)}$$

where R is the cavity radius. The pressure within the cavity is p, and at infinity $p_\infty$. At time t = 0 the radius is $R_o$. For the cavity collapse problem p = 0, and equation (1) can be manipulated into the following form

$$t = \frac{-R_o}{\sqrt{\frac{2}{3}\frac{p_\infty}{\rho}}}\int_{x}^{1}\frac{X^{3/2}dX}{\sqrt{1 - X^3}} \qquad \text{(II-D-2)}$$

where $X = R/R_o$. Note that the factor multiplying the integral has the dimensions of time and defines a characteristic time

$$\tau = \frac{R_o}{\sqrt{\frac{2}{3}\frac{p_\infty}{\rho}}} \qquad \text{(II-D-3)}$$

Two examples are shown in Figures 1 and 2. For both cases the collapse time is $t = 0.6\ \tau$. In terms of the characteristic time, the curve in

either figure is a universal curve for this problem. As a rule-of-thumb, cavity collapse is about 60% of the characteristic time.

Cavity Oscillation

When $p \neq 0$ in Equation (1), there occurs oscillations of the cavity. It is assumed that the compression and expansion of the trapped gas is adiabatic and lossless, i.e., isentropic. Consequently, pressure and cavity radius are related by

$$\frac{p}{p_o} = \left(\frac{R_o}{R}\right)^{3\gamma} \qquad \text{(II-D-4)}$$

where $p_o$ is the gas pressure when $R = R_o$. The ratio of heat capacities $C_p / C_v$ is symbolized by $\gamma$. Introduction of Equation (4) into Equation (1) yields

$$\frac{t}{\tau} = \int_Z^1 \frac{dZ}{Z^2 \left[Z^3 (\alpha + 1) - \alpha Z^{3\gamma} - 1\right]} \qquad \text{(II-D-5)}$$

where a new parameter $\alpha$ has been introduced. This parameter depends on initial ratio of pressures within the cavity and at infinity and is defined by

$$\alpha = \frac{p_o}{(\gamma - 1)\, p_\infty} \qquad \text{(II-D-6)}$$

In Equation (5) Z equals $R_o / R$ which should be noted is the reciprocal of X in Equation (2). A solution of Equation (5) is shown in Fig. 3. The complete curve cannot be obtained from a single integration. When $Z^3(\alpha + 1) - \alpha Z^{3\gamma} - 1 = 0$, the integrand approaches infinity. This occurs when a maximum or minimum in radius or pressure is attained.

At this point a new set of $R_o$ and $p_o$ values are introduced and integration proceeds.

For the example of Fig. 3, the pressure starts at $p_o/p_\infty = 6.67$ and $Z = 1$. When $p/p_\infty = 0.4$ at $Z = .80$ the integrand approaches infinity. This is at the minimum of the $p/p_\infty$ trace. One continues at this point letting $p_o/p_\infty = 0.4$ and a new Z defined as 1.000. Integration then continues to get the portion of the curve from minimum $p/p_\infty$ to maximum $p/p_\infty$, i.e., the part of the curve with positive slope. For the case of $\alpha = 16.675$, one cycle of oscillation requires a time of $1.35\tau$.

In the interpretation of Fig. 3 note that large $p/p_\infty$ occurs for small R or large Z. Although $0.4 \leq p/p_\infty \leq 6.67$ in Fig. 3, the range of radius is $0.64 \leq R/R_o \leq 1.24$. Large variations in $p/p_\infty$ are caused by small changes in $R/R_o$ due to $3\gamma$ power dependence.

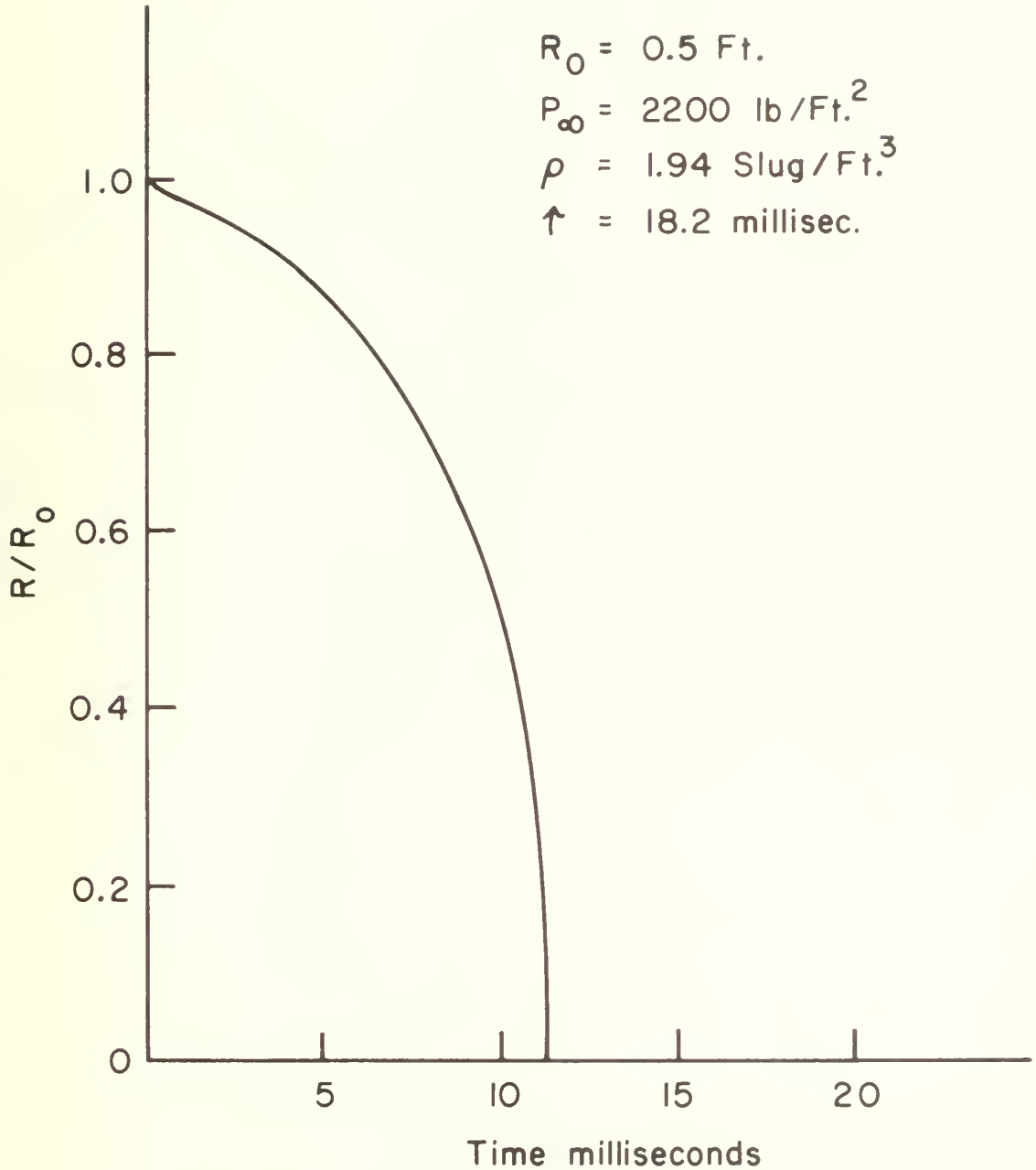


Fig. II-D-1 Cavity Collapse Time from an Initial Radius of 0.5 Foot.

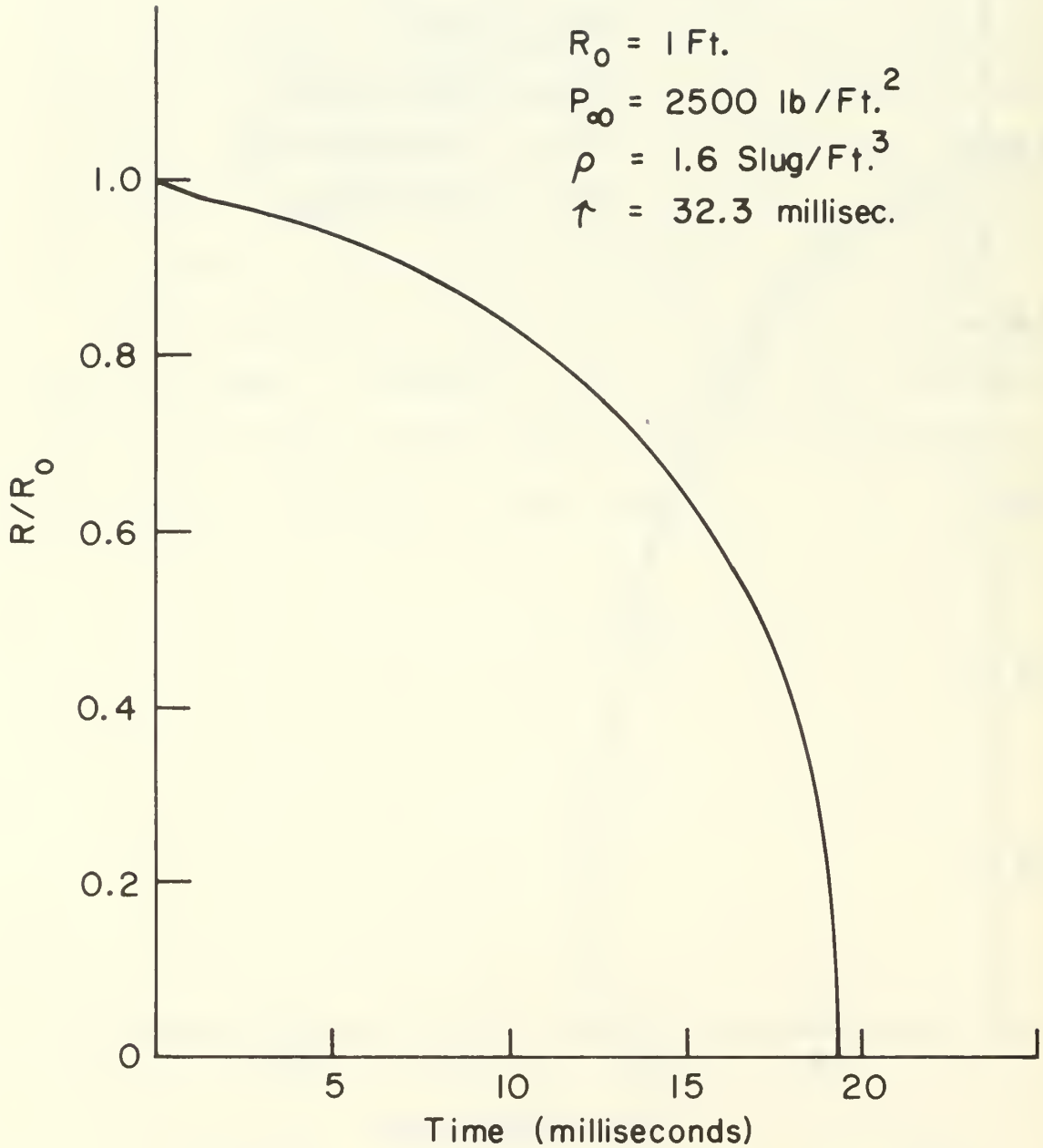


Fig. II-D-2 Cavity Collapse Time from an Initial Radius of 1.0 Foot.

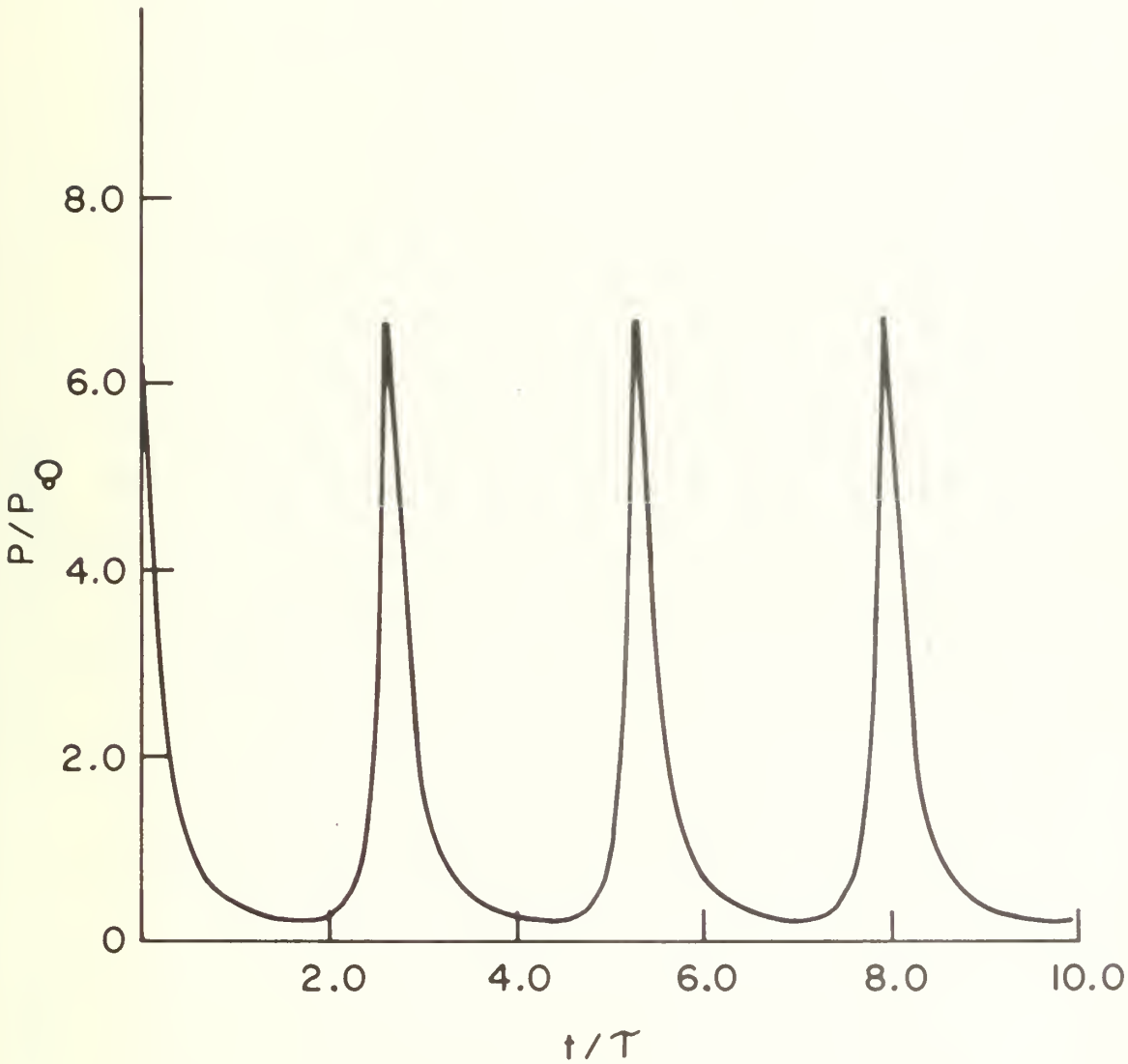


Fig. II-D-3 Hydraulic Ram Cavity Pressure Oscillation.

# III. HYDRAULIC RAM EXPERIMENTAL FACILITIES

## A. Introduction

The design, fabrication, and calibration of a ballistic range for aircraft survivability studies was accomplished under the present contract. The range was designed specifically with the hydraulic ram problem in mind. Of paramount importance was a consistently accurate method for determining a time history of the projectile velocity before projectile-tank impact and during hydraulic ram events that occur after penetration. Since projectile attitude at entry is important, shadowgraph stations were required along the flight path to make an estimate of projectile attitude. Two shadowgraph stations were also required to picture the hydraulic ram phenomenum as a function of time within the tank. The shock wave system, projectile position, and cavity shape and size could be determined using this data. The electronics associated with the ballistic range was designed to give stable, repeatable measurements at very small time intervals. Calibration of the present range components has shown that consistently accurate data is obtained. As a result, a reliable means of obtaining projectile energy as a function of time during hydraulic ram has been accomplished.

B. Ballistic Range Components

Basic elements of the ballistic range are shown in Figure III-B-1. The rifle mounting system is composed of the rifle mount and stand. The rifle mount was adjustable in azimuth (+ 8 degrees) and elevation (+ 3 degrees to - 5 degrees) for ease in boresighting. Rifles of 22.2 and 30 caliber may be used. Figure III-B-2 shows the complete rifle mounting system and Figure III-B-3 shows the rifle mount in detail.

The shadowgraph stations are composed of a bullet sensor, time delay unit, spark source, collimating lens, and a shadow box with reference grid for mounting the Polaroid film holder. Figure III-B-4 shows a typical shadowgraph station. The bullet sensor is a chronograph screen that has a five volt D.C. signal shorted to ground across it. The bullet sensors provide start and stop pulses to the counters and delay circuits. The delay units generate time delayed pulses ranging from 190 μs to 1700 μs that trigger spark sources. Figure III-B-5 shows the delay unit circuitry. Figures III-B-6 and -7 shows typical shadowgraphs taken along the bullets' trajectory before impact. The complete ballistic range configuartion is shown in Figures III-B-8 and -9. The bullet catcher is shown in Figure III-B-10.

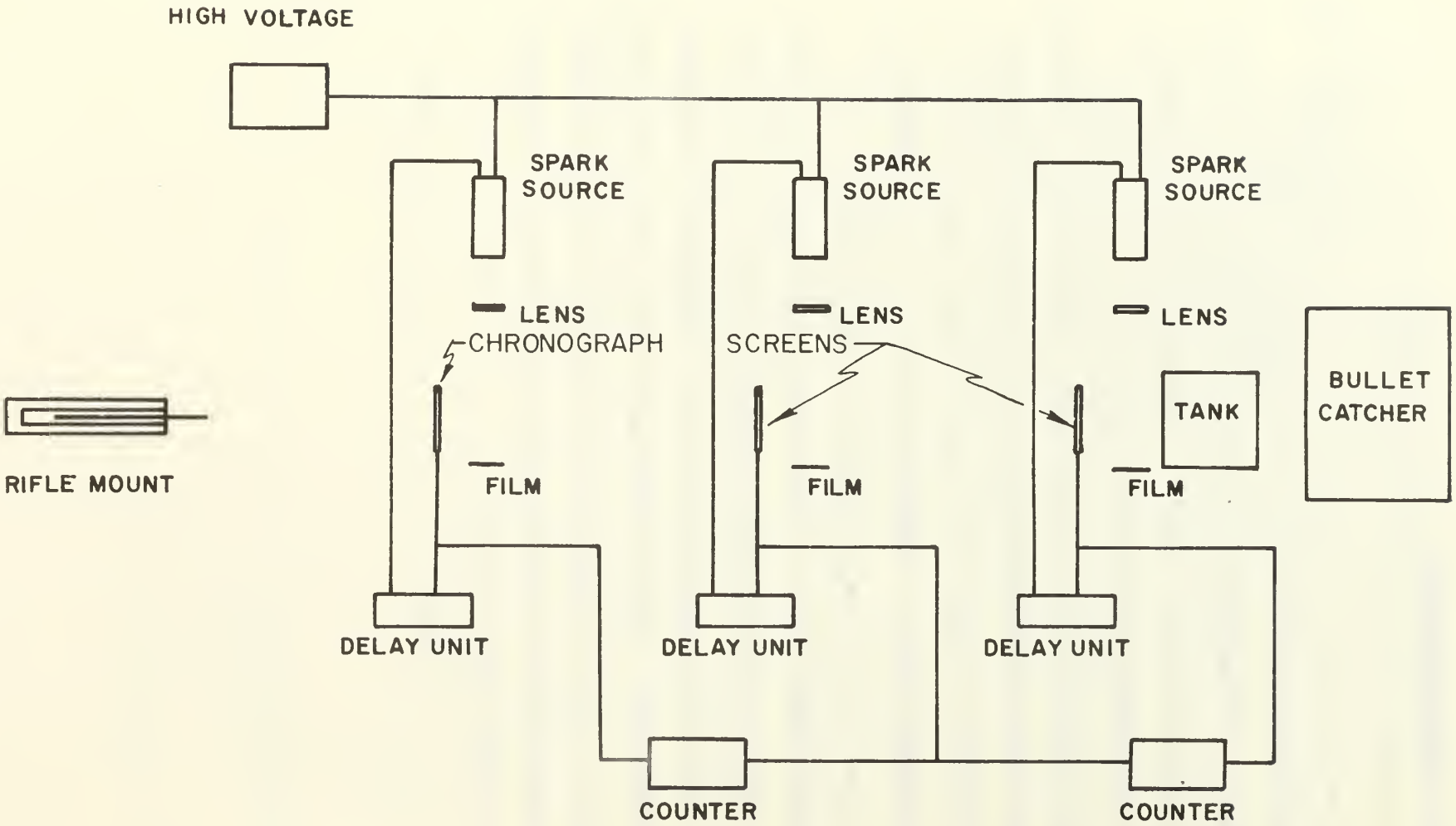


FIGURE III-B-1
BALLISTIC RANGE COMPONENTS

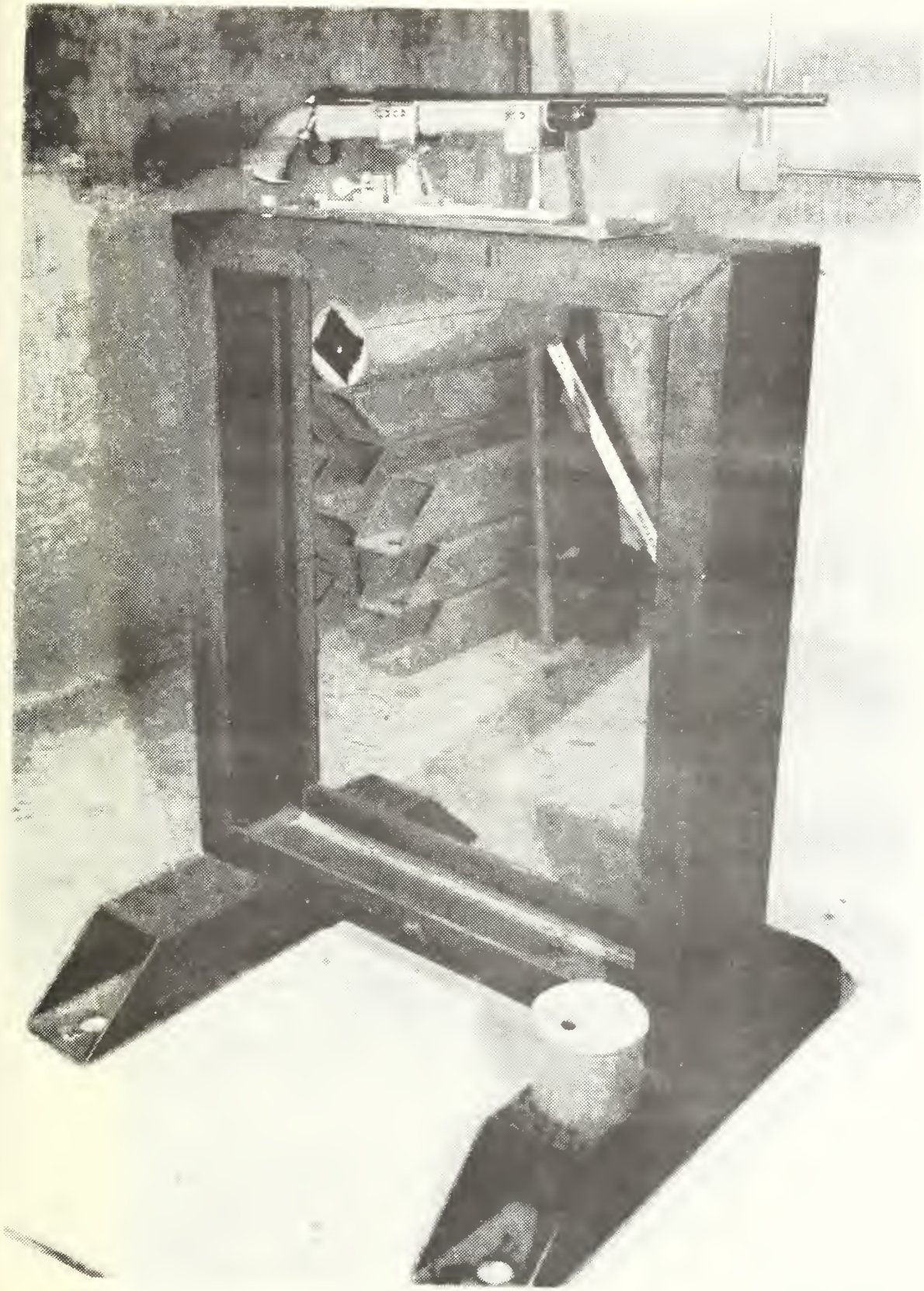

Figure III-B-[illegible] Ballistic Range Rifle Mounting Syste[illegible]

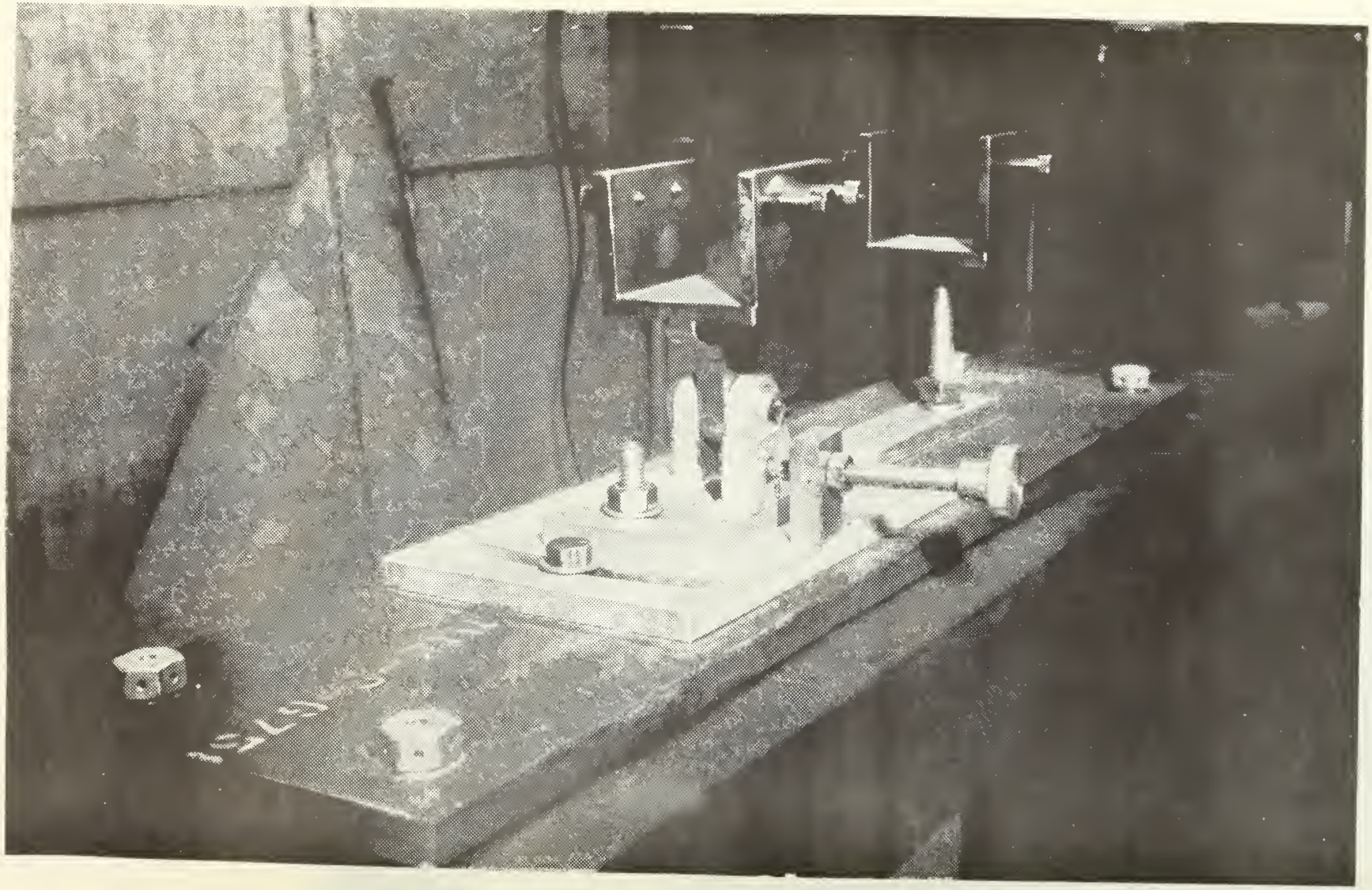

Figure III-B-3 Ballistic Range Rifle Mount

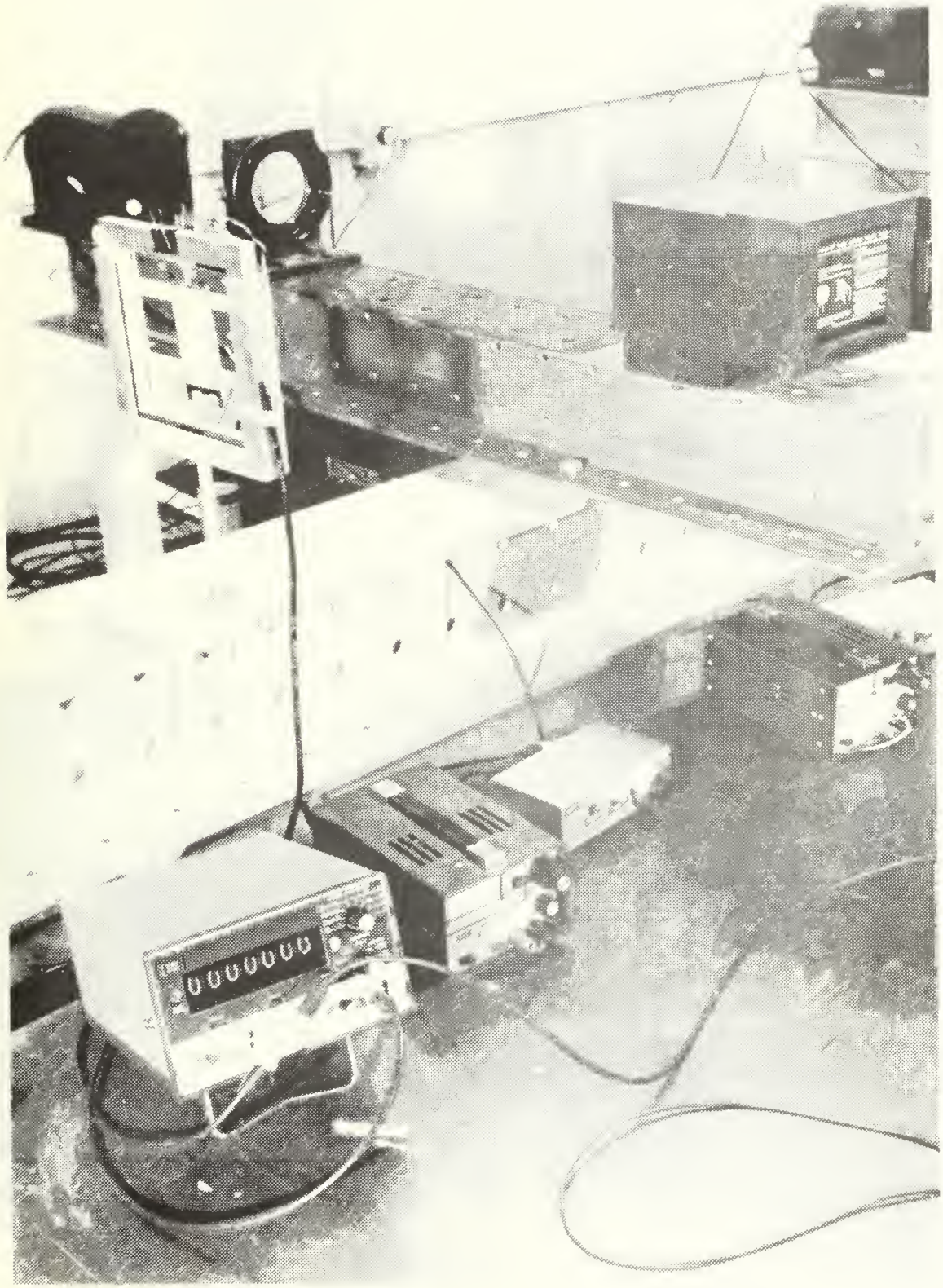

Figure III-B-4 Ballistic Range Shadowgraph Station.

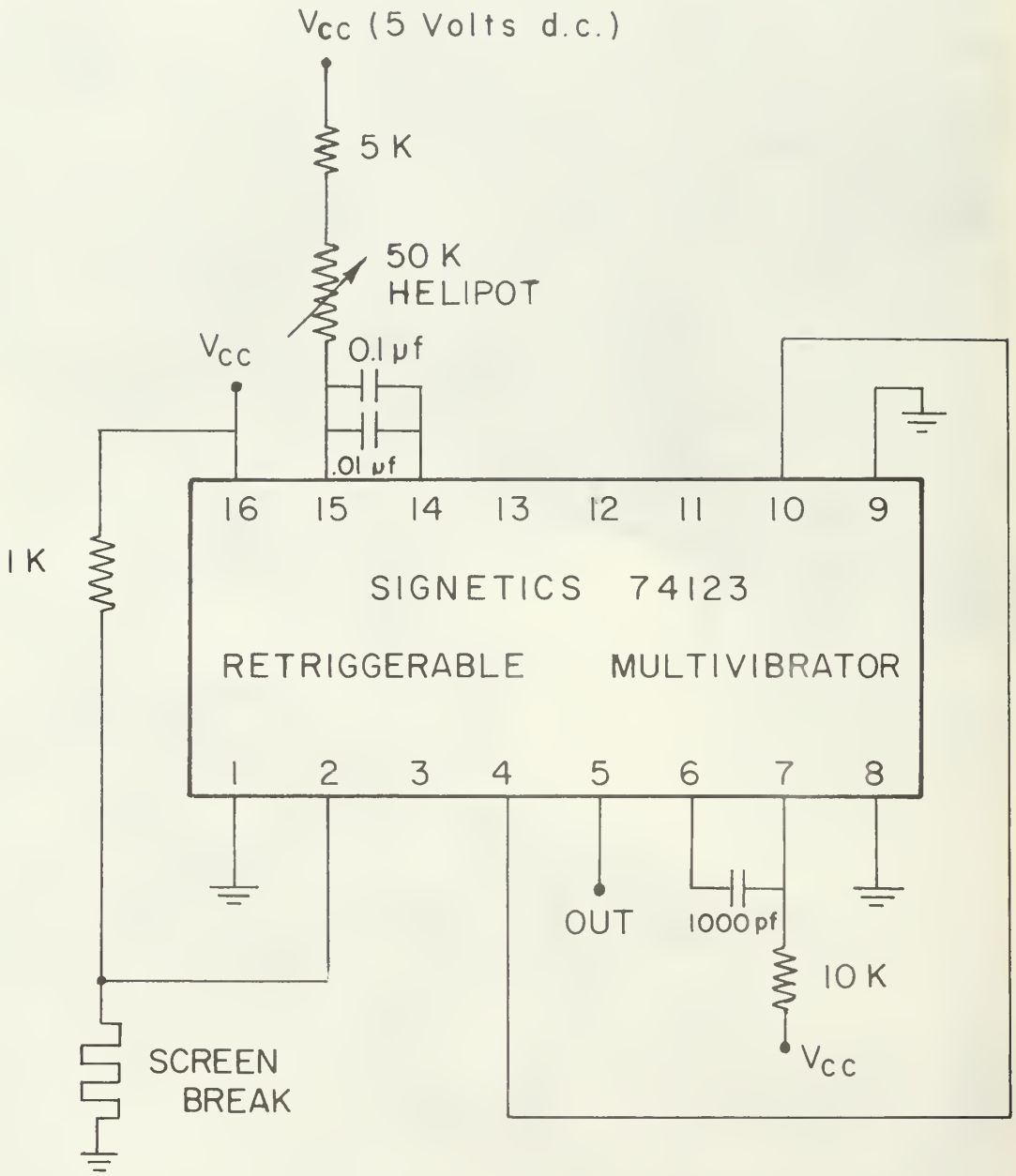


FIGURE III-B-5 DELAYED PULSE GENERATOR CIRCUITRY (VARIABLE)

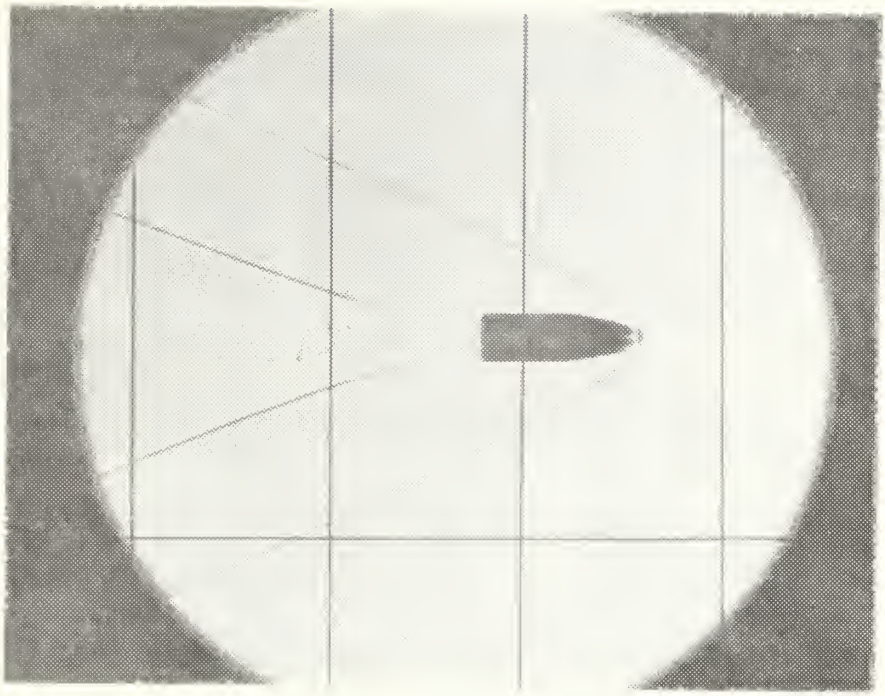

Figure III-B-6 Shadowgraph of a 63gr Semi-Point with a Velocity of 2941 fps.

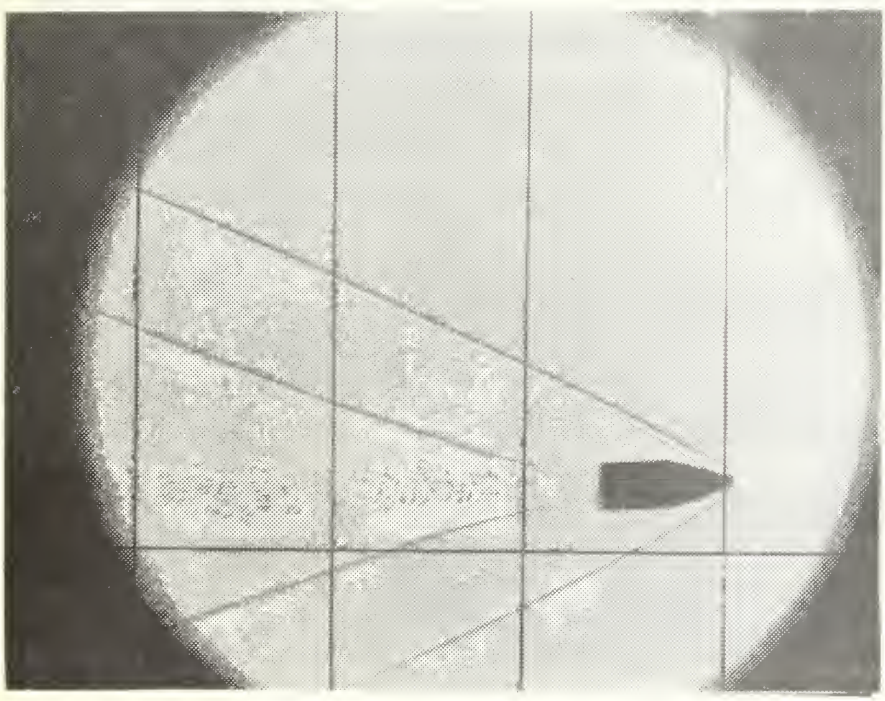

Figure III-B-7 Shadowgraph of a 50gr Spitzer Used in Range Calibration with a Velocity of 3080 fps.

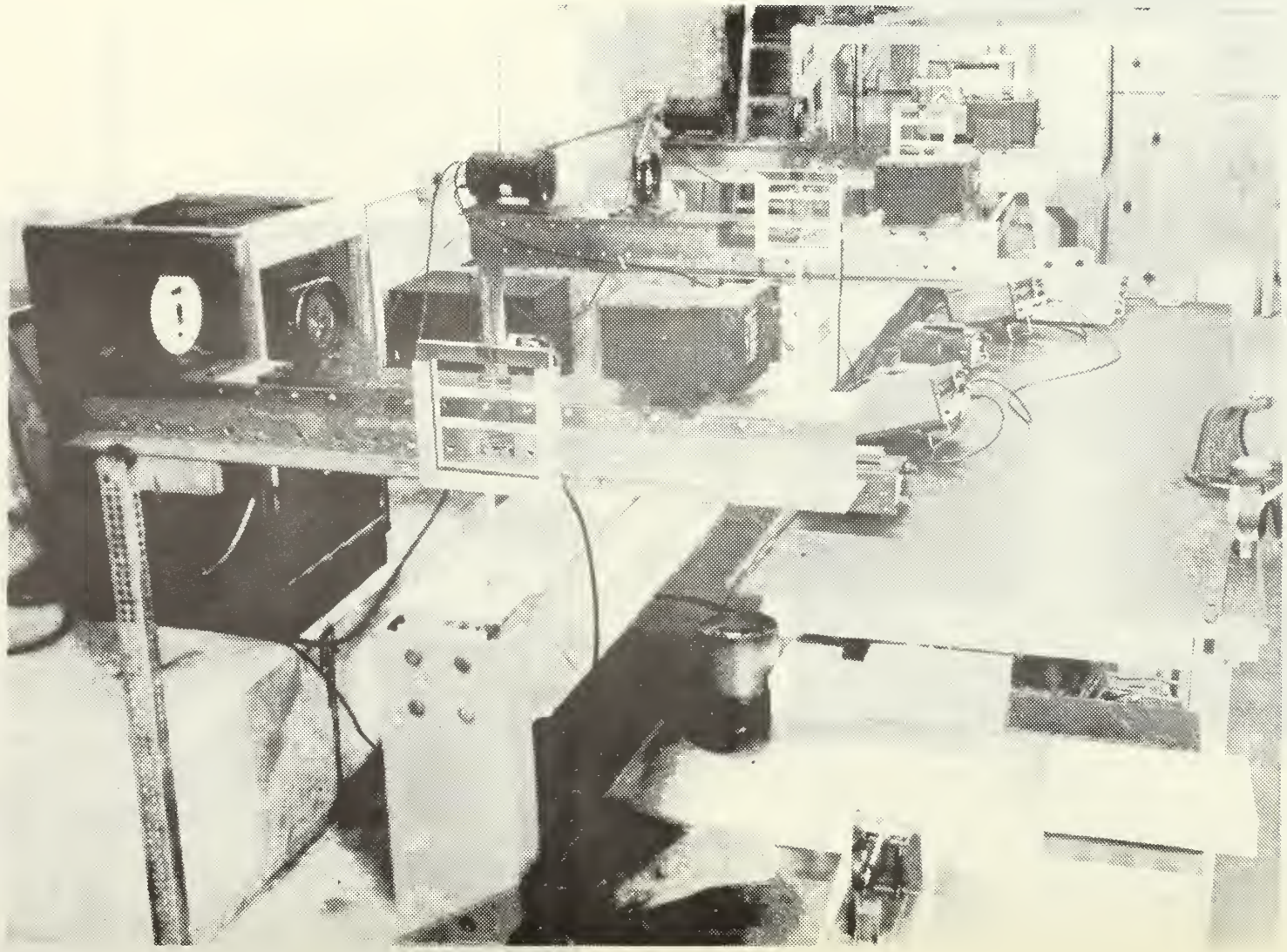

Figure III-B-8 Ballistic Range Configuration (Down Range View).

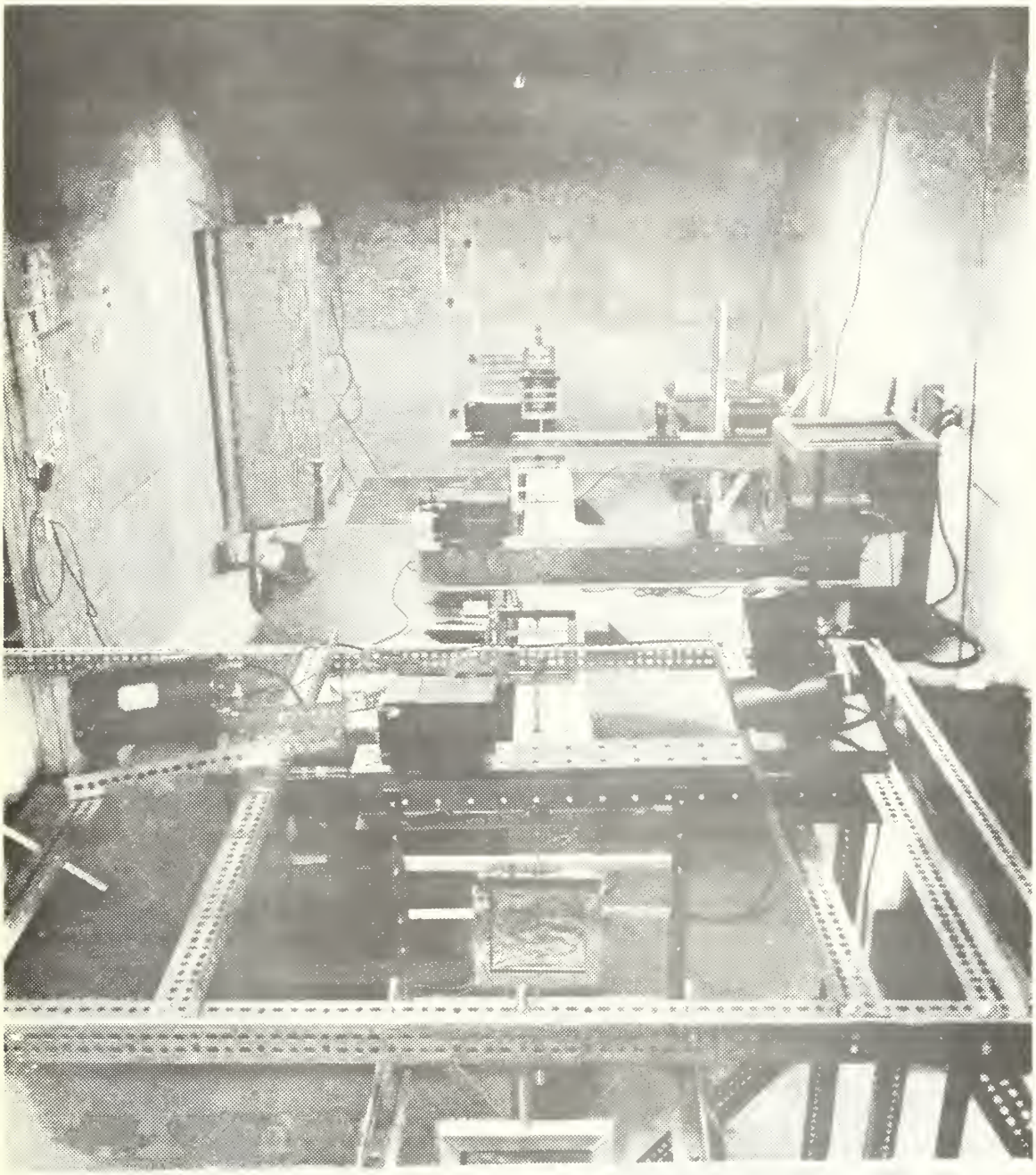

Figure III-B-9 Ballistic Range Configuration (Up Range View).

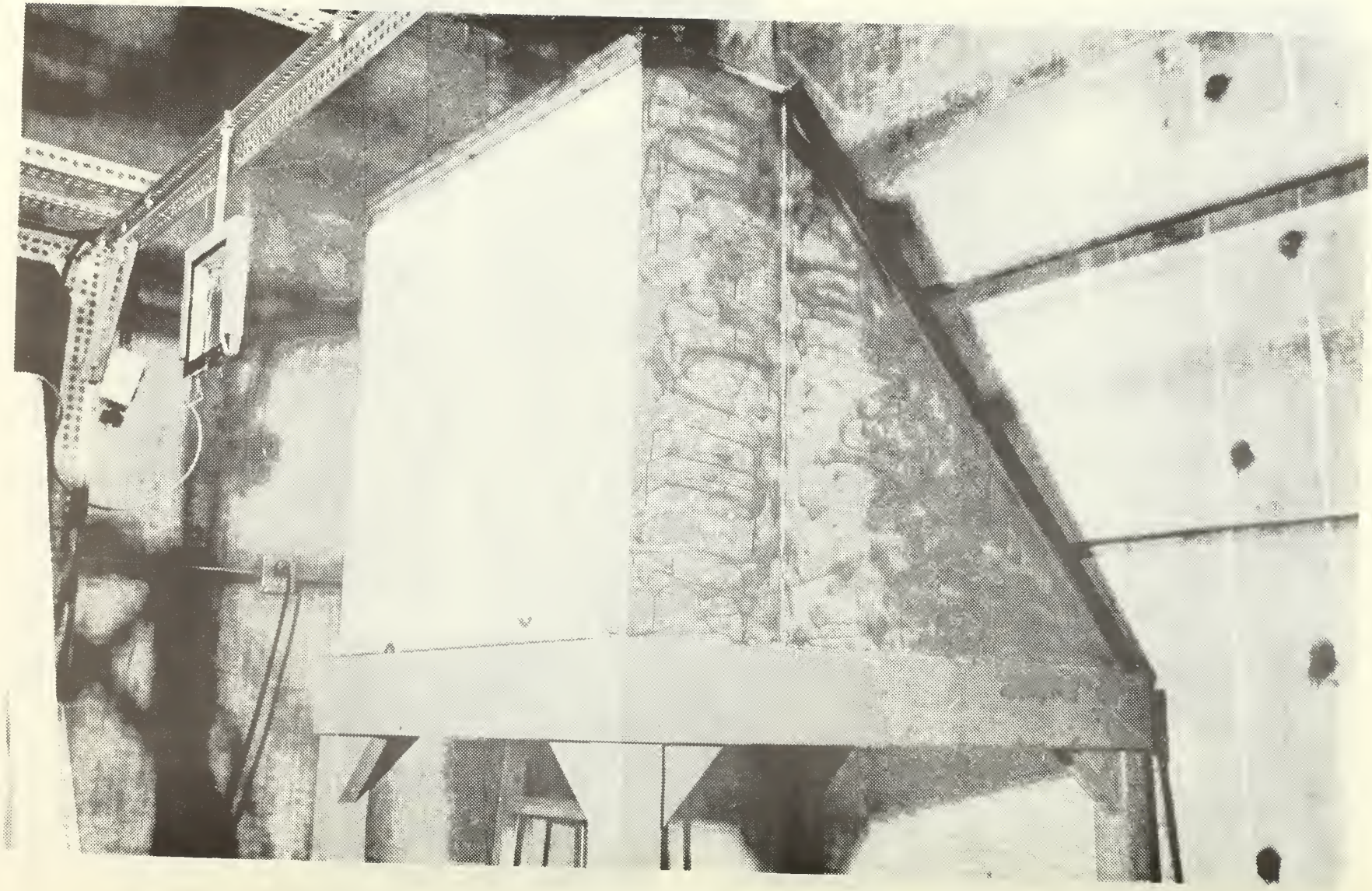

Figure III-B-10 Ballistic Range Bullet Catcher.

C. Experimental Apparatus

The experimental program was divided into three phases. The first phase consisted of measurements of the projectile energy loss during impact with the wall of an empty tank. Phase II measurements were taken with a water-filled tank but with the projectile entering the tank through a prepunched hole. Phase III measurements were taken using solid entry walls with a fluid-filled tank. A comparison of these results make it possible to partition the energy losses of each of the various hydraulic ram component dissipative processes. Figure III-C-1 shows the test apparatus for Phase I. A test plate is positioned with two bullet sensors mounted directly behind. The average velocity after plate penetration is measured and the interaction phenomenum may be studied using a shadowgraph.

Phase II and III testing uses the test setup shown in Figure III-C-2. Two shadowgraph stations provide for a photographic record of hydraulic ram phenomenum at two preset times after projectile impact. Figure III-C-3 shows the plexiglass side wall tank with its removable entry and exit walls. The entry and exit walls are fastened to the 1 inch plexiglass side walls by studs that pass through steel clamping frames which sandwich the test plate. The tank is a cube with 18 inch inside dimensions. The electronic delay and spark source trigger circuits used for the tank shadowgraph are similar to those shown in Figure III-B-5. Station one timing starts at the last downrange shadowgraph station sensor and its delay circuit range is variable from 200 μs to 1650 μs. Station two timing starts when the station one spark source fires and another delay circuit is used to fire the station two spark source from 3 μs to 20 μs later.

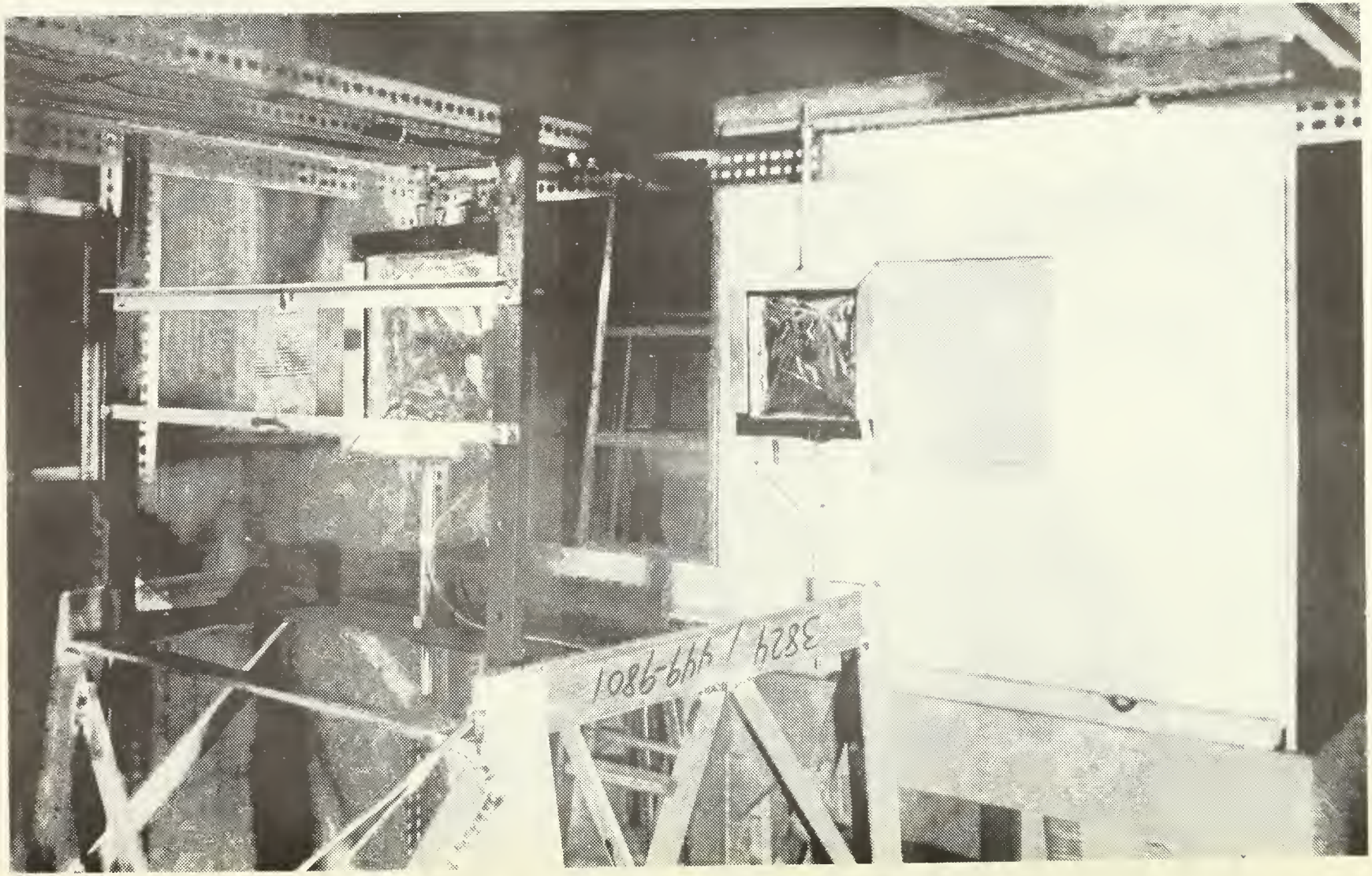

Figure III-C-1 Test Specimen Setup.

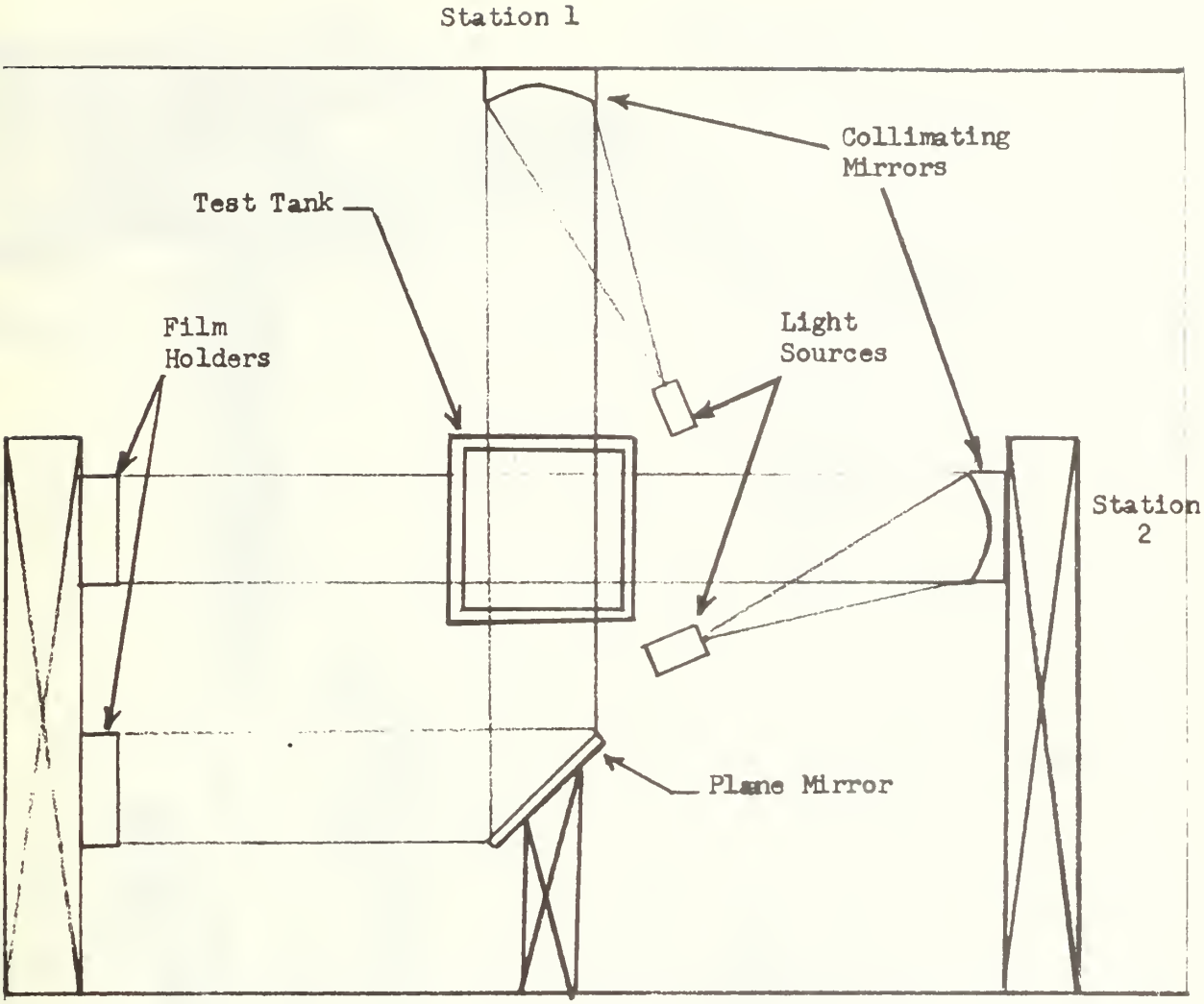


Schematic of Shadowgraph Apparatus

Station 1 Station 2

Fig. III-C-2 Fuel Tank Test Setup

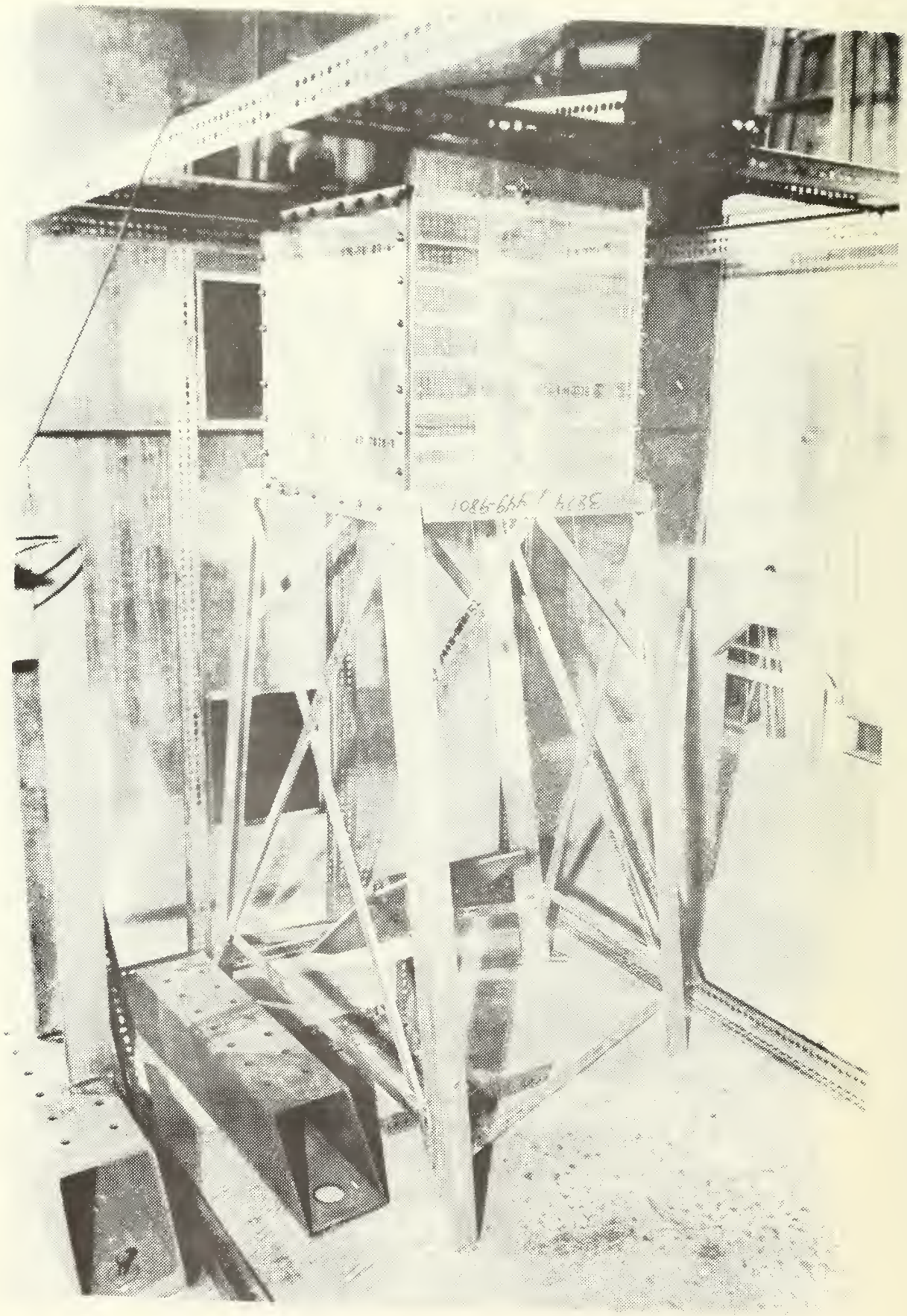

Fig. III-C-3 Test Tank and Stand

# IV. TEST RESULTS TO DATE

## A. Penetration Studies

Phase I testing was conducted to gain some useful knowledge of the fuel tank wall-projectile penetration characteristics. Metal plates of 7075-T6 aluminum of thicknesses o.05, 0.09, and 0.16 inch were used. Projectiles of three masses and three nose shapes were fired into these plates at varying initial velocities using a .222 Remington rifle. The projectile velocity was measured before and after the plate penetration. All projectiles studied were stable before impact and entered the test plate perpendicular. Several shots at each mass, nose shape, and velocity were made to provide statistical data in order to determine the energy lost by the projectile during penetration of the entry wall without fluid support. The energy loss thus determined will be the same as the energy lost during a similar event in hydraulic ram except for the effects of fluid foundation and damping. Phase II testing will yield the amount of energy initially lost to the fluid with entry wall-fluid interactions but with no penetration effects. Phase III testing will yield the total initial energy loss during penetration. Comparisons of Phase II and Phase III should yield the energy loss during entry wall penetration with fluid effects. Comparison of these results with Phase I should then yield the difference in energy loss due to the presence of the fluid medium.

To date the Phase I testing has been accomplished (Ref. 8) for the 0.09 inch thickness plate only. At the present time test data for the other two wall thicknesses is being taken. Plans also include similar testing using 30 caliber projectiles in the near future.

Figure IV-A-1 shows a typical projectile flowfield after plate

penetration. Spallation occurs from the back face of the entry wall producing small supersonic fragments that travel behind the projectile bow shock. A nearly spherical strong shock wave propagates into the tank from the projectile point of entry during the initial stage of plate penetration. Shortly after bullet passage through the plate, the bullet bow shock wave catches up to the original spherical wave. These waves coalesce and the resulting bullet bow shock wave has a reflex shape.

Previous work by Forman (Ref. 9) derived equations for the minimum penetration velocity (ballistic limit) and the projectile exit velocity. The ballistic limit is given by:

$$V_o = \sqrt{\frac{2\pi Gr}{15m}\,(1.6t - 4/3)} \qquad \text{(IV-A-1)}$$

where G is the material shear modulus, r is the radius of the hole produced in the plate (assumed to be the same as the radius of the projectile), t the wall thickness, and m is the projectile mass. For impact velocities greater than $V_o$ the exit velocity $V_e$ approaches the impact velocity. Assuming a constant energy loss the exit velocity may be found by:

$$V_e = V_o \sqrt{\left(\frac{V_i}{V_o}\right)^2 - 1} \qquad \text{(IV-A-2)}$$

where $V_i$ is the impact velocity. Equations (1) and (2) are independent of nose shape and assumed that the kinetic energy loss is independent of impact velocity for impact velocities greater than the ballistic limit. Figure IV-A-2 shows the results of firing projectiles of constant mass but different nose shapes. The data for both shapes agree closely with the theoretical predictions. This indicates that nose shape has a minor role in determining the exit velocity. Figures IV-A-3 and -4 show the

result of tests using projectiles of different mass with the same nose shape. These tests again showed excellent agreement with theory over the tested range of impact velocities. The greater length of the 63 gr. projectiles increase the effect any yaw or spin axis nutation has at plate impact. If entry is not perpendicular, damage is more severe and energy loss due to penetration is greater. A plot of kinetic energy loss versus initial velocity for all projectiles is shown in Figure IV-A-5. The theoretical energy loss is invariant with initial velocity and is shown as a reference. The energy loss associated with high mass projectiles is typically greater than that of the lower mass projectile for equal initial velocities as expected.

Inspection of the damage to the entry walls shows that maximum damage occurs at a velocity slightly higher than the ballistic limit and the damage size approaches the diameter of the bullet as the impact velocity increases from the ballistic limit.

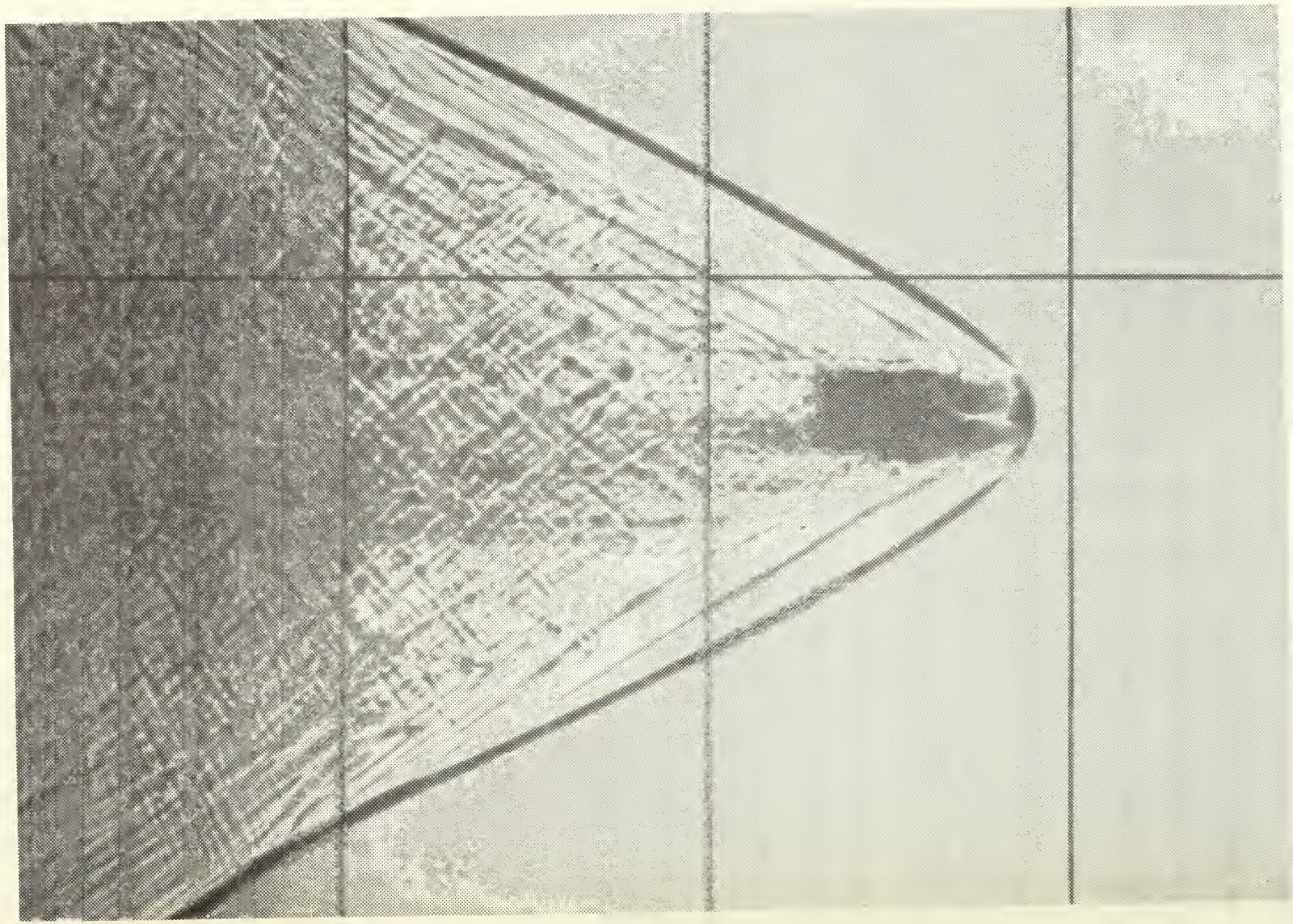

Figure IV-A-1 Flow Field after Plate Penetration.

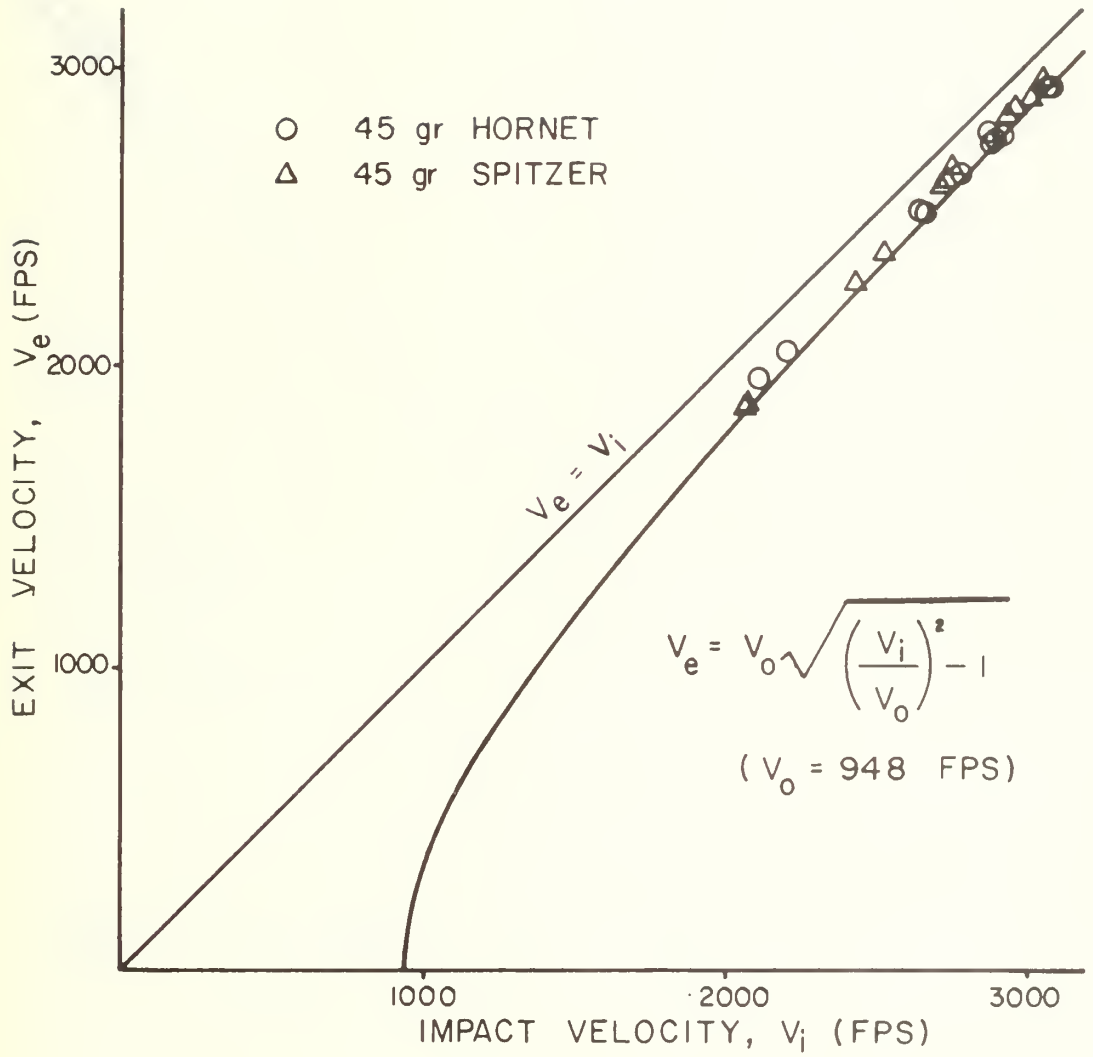


Fig. IV-A-2 Exit Velocity versus Impact Velocity for Two 22.2 Caliber Projectile Shapes Fired Normal to a 0.090 inch Thick 7075-T6 Aluminium plate.

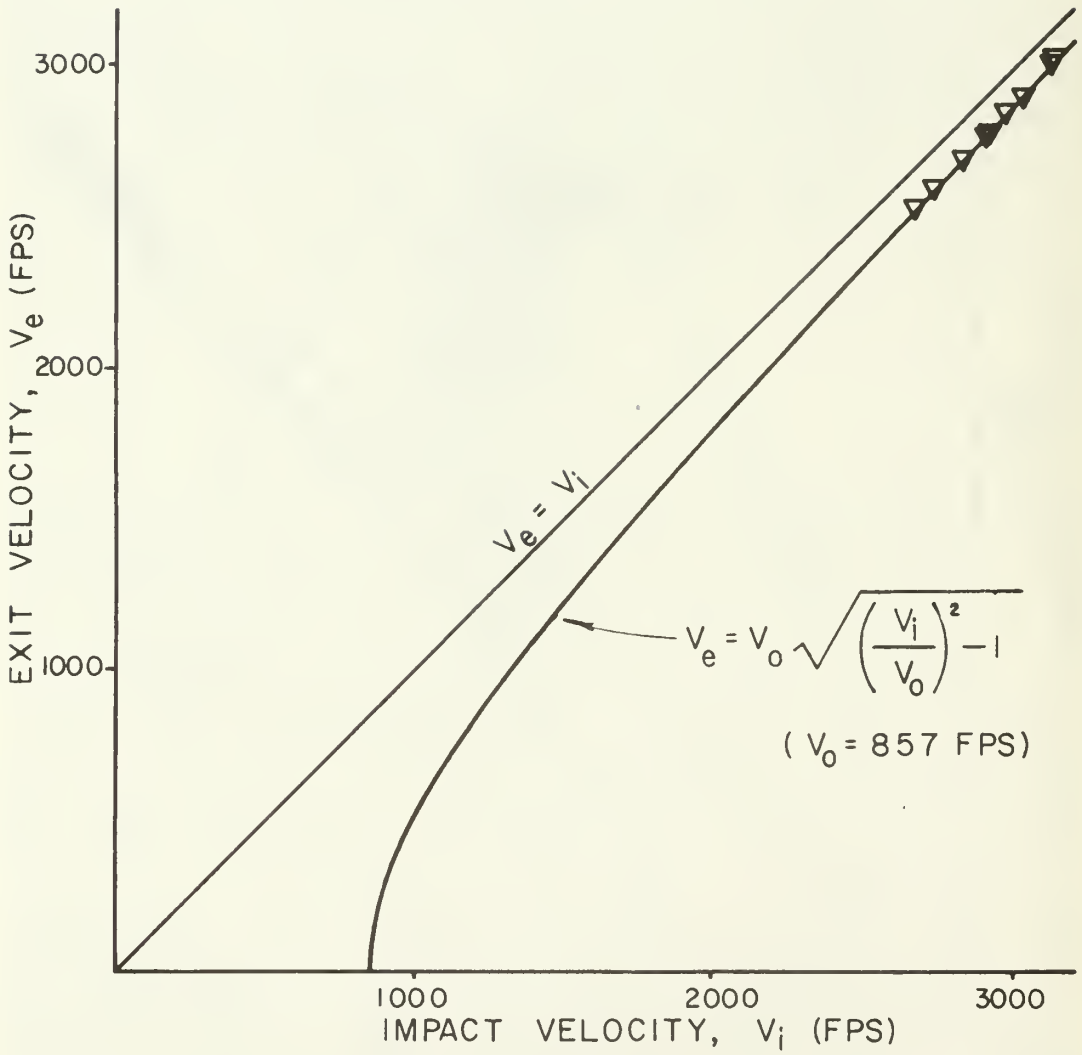


Fig. IV-A-3 Exit Velocity versus Impact Velocity for a 55gr Semi-Pointed 22.2 Caliber Projectile Fired Normal to a 0.090 inch Thick 7075-T6 Aluminium Plate.

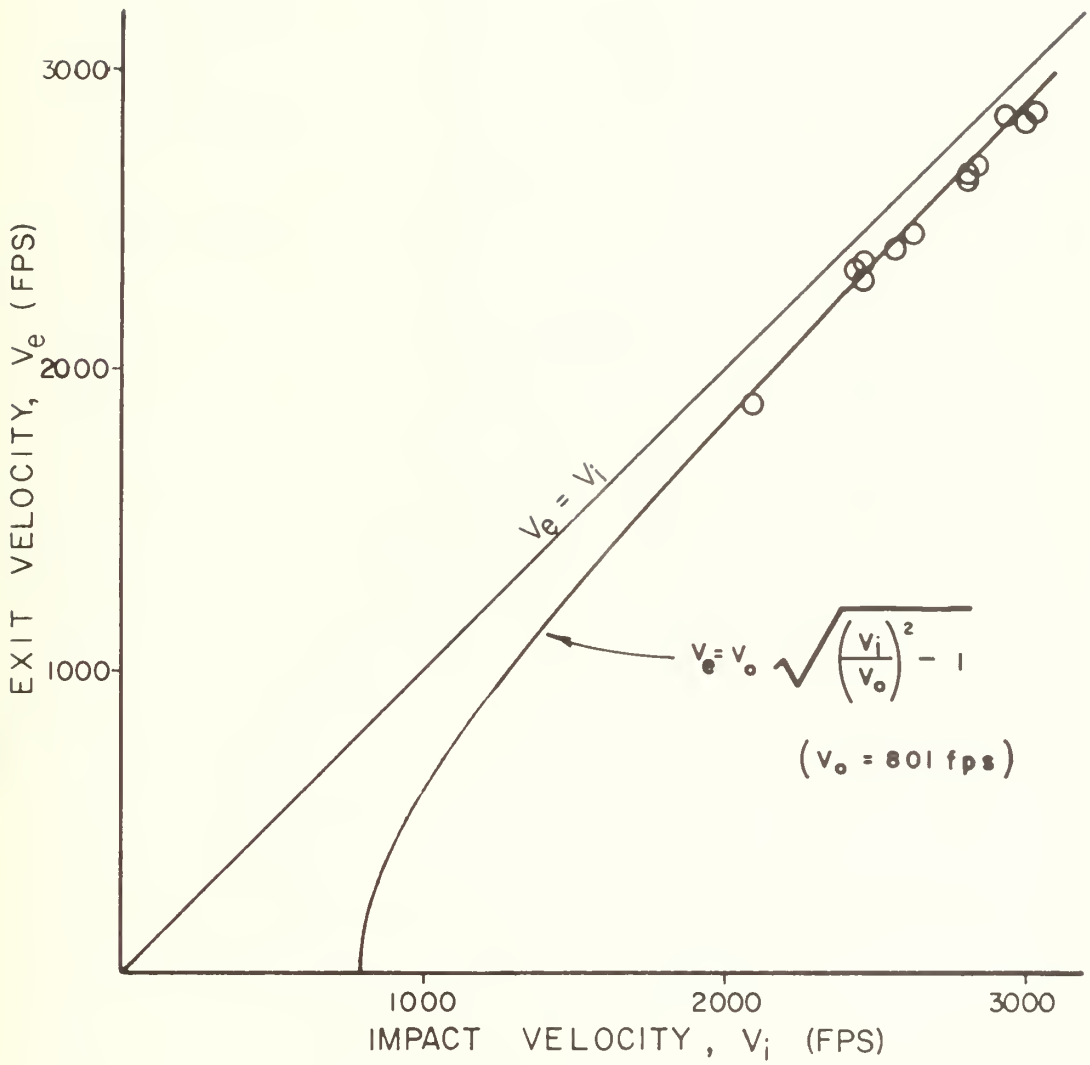


Fig. IV-A-4 Exit Velocity versus Impact Velocity for a 63gr Semi-Pointed 22.2 Caliber Projectile Fired Normal to 0.090 inch Thick 7075-T6 Aluminium Plate.

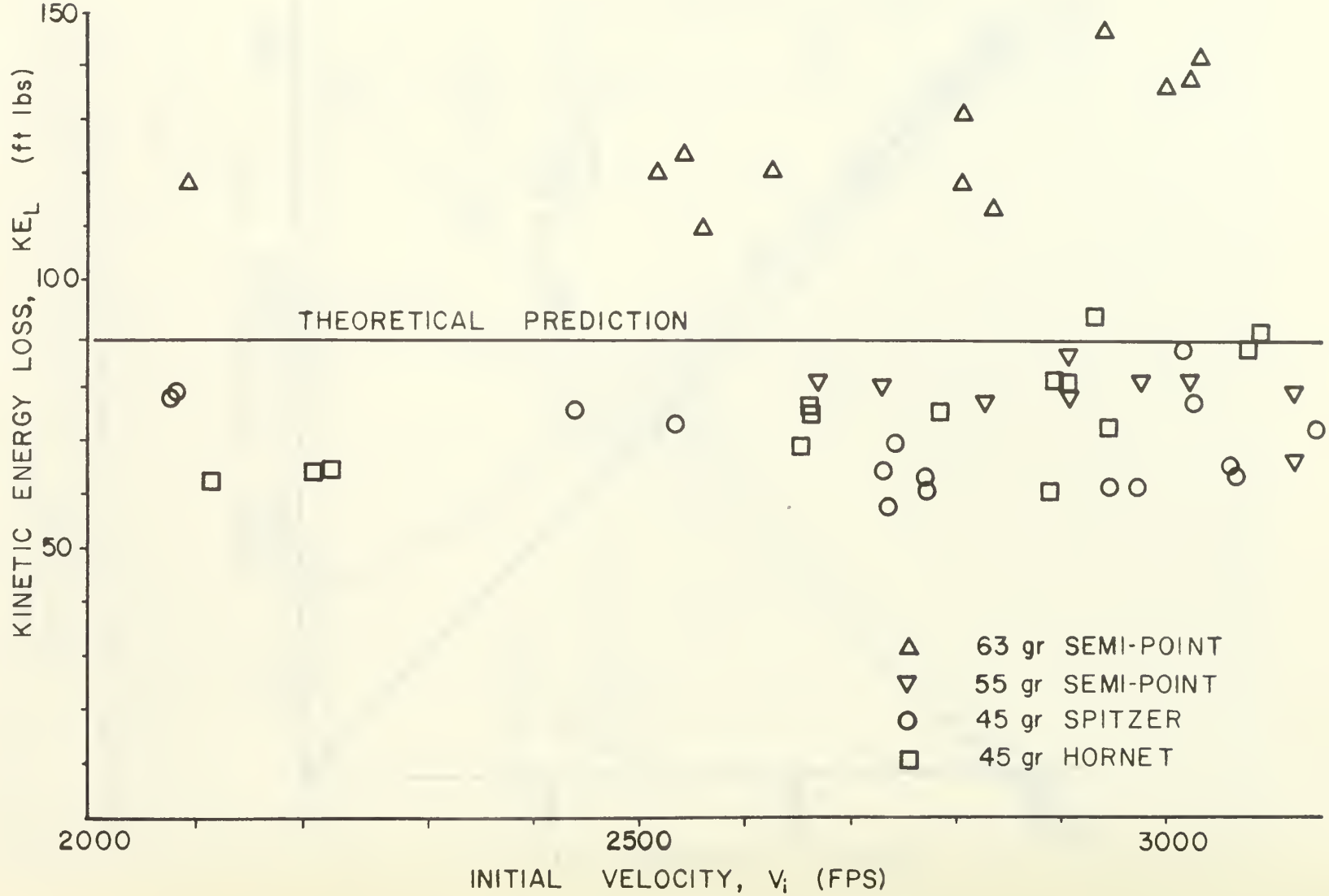


Fig. IV-A-5 Plot of Kinetic Energy Loss versus Initial Velocity for a Range of Projectile Masses and Shapes.

B. Shock Phase Studies

Phase II and III studies of the shock phase of hydraulic ram to date have been limited to low energy .22 caliber shots. An attempt to increase kinetic energy level by using higher velocity .222 ammunition resulted in catastropic failure of the test tank as shown in Figure IV-B-1. The failure of this tank design to withstand hydraulic ram pressure loadings is a regrettably graphic example of the magnitude of the survivable fuel tank design problem. Inspection of the wall fracture shape seems to indicate that hydraulic ram tensile loads, concentrated locally by the side wall stud threads, produced failure. It can also be deduced that since the front wall sustained the major damage, shock phase pressures can significantly reduce the ability of fuel tank front walls to survive the later phases of hydraulic ram.

In spite of the test tank destruction, much useful information has been gathered on the shock phase of hydraulic ram. Dual spark shadowgraphs of the tank were taken at varying times after projectile impact. These data provided information on the characteristics of the shock wave pressure pulse and the rate of energy loss of the projectile.

1. Shadowgraphs of Fuel Tank Flow Field

Phase II testing was conducted using a 1 inch diameter prepunched hole in a .09 inch thick entry wall. Figure IV-B-2 illustrates typical results of the impact by a 1.95 gram lead bullet at a velocity of 0.374 kilometers per second (1226 ft/sec) into the water-filled test tank. The photographs of Figure IV-B-2 show that a hemispherical wave front is produced whose center is the point of impact. It is implied from this fact that projectile shape and forward momentum have no significant effect on the wave front motion during the early stages of hydraulic ram. Inspection of the wave thickness also shows that the

shock front strength varies along the wave. The greatest strength occurs in the direction of projectile flight and the least strength occurs where the shock and wall meet.

Phase II testing involved impacts with standard factory loaded .22LR ammunition. Average velocities of the resulting shock waves were determined from shadowgraphs similar to those in Figure IV-B-2. The shadowgraphs were used to determine time and position of the shock wave as it propagated through the fluid. The slopes of the resulting time-distance plots yielded propagation velocities of the shock. Figure IV-B-3 in such a plot of shock front velocity for a projectile with an averaged impact kinetic energy of 135.2 Joules. The plot shows that the shock front velocity decays to the acoustic speed in water (1.5 kilometers per second or 4920 ft per second) at a distance of about 11 centimeters (4.3 in).

Pressures generated in the water at the shock front corresponding to the measured shock front velocities were determined from data given in Table 2.2 in Ref. 10. Figure IV-B-4 shows these shock front pressures. Extremely high pressures are generated in the water near the impact point and decay rapidly due to geometric expansion of the shock front. For example, Figure IV-B-4 shows that at a distance of 2.24 centimeters (0.88 in) from the impact point the resulting shock front pressure is 3750 kilograms per square centimeters (53,335 $lb/ft^2$). As with any object moving through a fluid, the projectile creates a dynamic pressure in the water due to the stagnation conditions on the front surface. Pressures of 710 kilograms per square centimeter ($1.01 \times 10^4$ $lb/in^2$) were found to exist in the vicinity of the projectile during these studies. Figure IV-B-5 shows the evolution of the pressure field behind the shock front as a function of time. When the projectile

first penetrates the wall a strong shock is created and decays in strength as it propagates outward. At time $t_A$ the pressure behind the shock greatly exceeds the stagnation pressure on the projectile nose. Comparing pressures at $t_A$ and $t_B$ it is apparent that both shock front pressure and projectile stagnation pressure decay; however, the decay of shock front pressure is much more rapid. At time $t_C$ the stagnation pressure exceeds the shock front pressure. One could define the time where these pressures are equal as a characteristic time separating the shock and cavity phases of hydraulic ram. The characteristic time for the conditions of the test was found to be 32 microseconds.

Figure IV-B-6 illustrates the later stages of cavity growth and projectile speed decay. The air-filled cavity behind the projectile is opaque to light and casts a sharp shadow. The true shape of the cavity is not that of the shadow because of light ray refraction through the test setup. The spark shadow of the cavity is wider than the true cavity size which could be found using X-ray shadowgraph techniques. The projectile shadow is not visible but its position may be inferred by the position of the bright cusp of light present at the leading edge of the cavity shadow. This cusp is formed by light bent around the projectile. This bending is caused by changes in fluid refractive index. It is expected that the position of the nose of the projectile corresponds to the tip of the cusp. Using this technique, measurements were made of the progress of the projectile through the tank after impact.

A detailed analysis of projectile velocity decay is extremely difficult because of the many variable parameters. Assumptions must be made to account for the changes in projectile shape, drag coefficient, and attitude. Because of these difficulties a simplified analysis was made. If the projectile drag is given by

$$D = -m \frac{dV}{dt} = \frac{1}{2} \rho_f V^2 C_D A \qquad \text{(IV-B-1)}$$

the assumption of constant area, drag coefficient equal to one and constant projectile mass results in the following projectile velocity decay:

$$\frac{V}{V_o} = \exp\left[ - \frac{\rho_f C_D A x}{2m} \right] \qquad \text{(IV-B-2)}$$

Figure IV-B-7 and IV-B-8 show a comparison of experimental data with the previous analytical results for velocity and energy decay as a function of distance traveled by the projectile. This comparison indicates that in spite of the simplifying assumptions, the agreement between calculated and experimental values of velocity and energy after impact was good. In the experimental tests the projectile underwent a continual deformation during deceleration into the tank. The increase in frontal area during the deceleration was approximated by using an average final projectile frontal area of 0.5 square centimeters.

Decay of the projectile kinetic energy can be directly related to the amount of energy being transferred to the fluid. The slope of the projectile energy curve gives the rate of energy transfer to the fluid, assuming no projectile deformation. The average energy transfer rate for the projectile tested was approximately 20.6 Joules per centimeter of fluid traversed.

Phase III testing was accomplished using techniques similar to those used in Phase II. The test entry wall was however, solid. Figure IV-B-9 illustrates typical results of the impact by a 1.95 gram lead

bullet at a velocity of .374 kilometers per second (1226 ft/sec). The photographs of Figure IV-B-9 show the obscuration of events interior to the shock wave. The shadowgraphs show a strong hemispherical wave front as in the "pre-punched" wall case. This hemispherical wave is however, interacting with another wave front which appears as a straight line oblique to the wall. This wave front was caused by the propagation of shear and dilatation waves moving through the metal wall at a faster rate than the waves through the water. This wave is created by the penetration stage punching action of the projectile and its rate of propagation was found to be proportional to the bulk sonic velocity (dilatation wave) for aluminum (6.2 km/sec.)

2. Deformation of Lead Projectile

Projectiles were recovered after each experimental test and were found to display a unique pattern of deformation. The deformation phenomenon was very consistent for projectiles impacting the fluid through pre-punched plates. Three examples of projectiles after this type of impact are shown in Figure IV-B-10. The extent of deformation was directly proportional to the impact velocity and all projectiles exhibited one flat side and an undeformed side. This type of deformation is the result of the dynamic stability of the projectile as it traverses the tank fluid. As shown in Figure IV-B-11 the dynamic stability of the projectile is maintained through the equilibrium of the pressure and inertia. The figure demonstrates the effect of an angular displacement of the projectile from the equilibrium position. The center of pressure moves upward on a slightly curved front surface with the stagnation point. This creates a restoring moment which returns the projectile to its original position. Projectiles which penetrated a solid entry wall did not demonstrate this deformation phenomenon.

Figure IV-B-12 shows these projectiles and the small aluminum cap that was punched out by the projectile passage through the entry wall. Figure IV-B-13 shows typical entry wall damage.

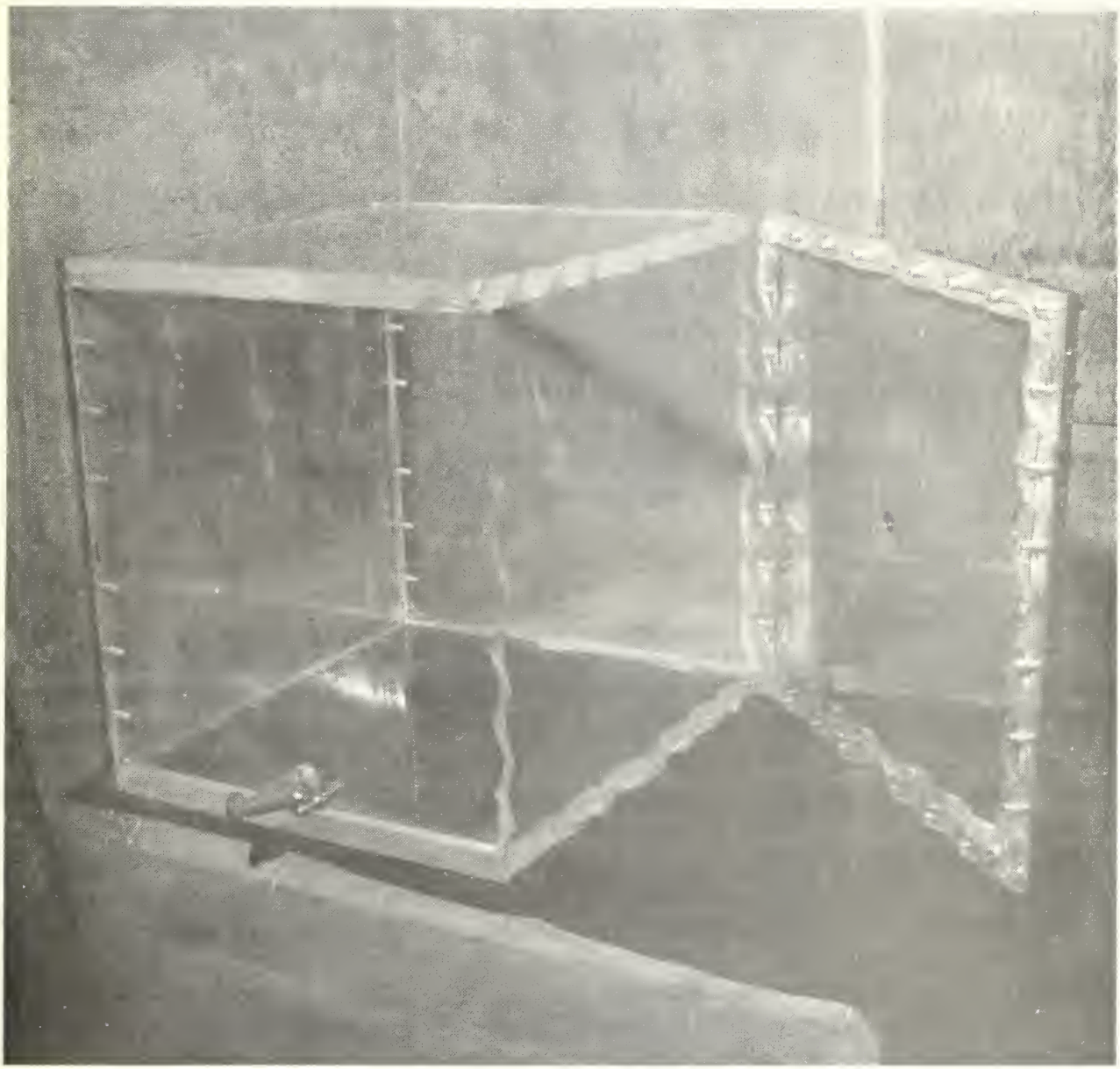

Figure IV-B-1: Test Tank After Impact of .222 Caliber High Energy Projectile

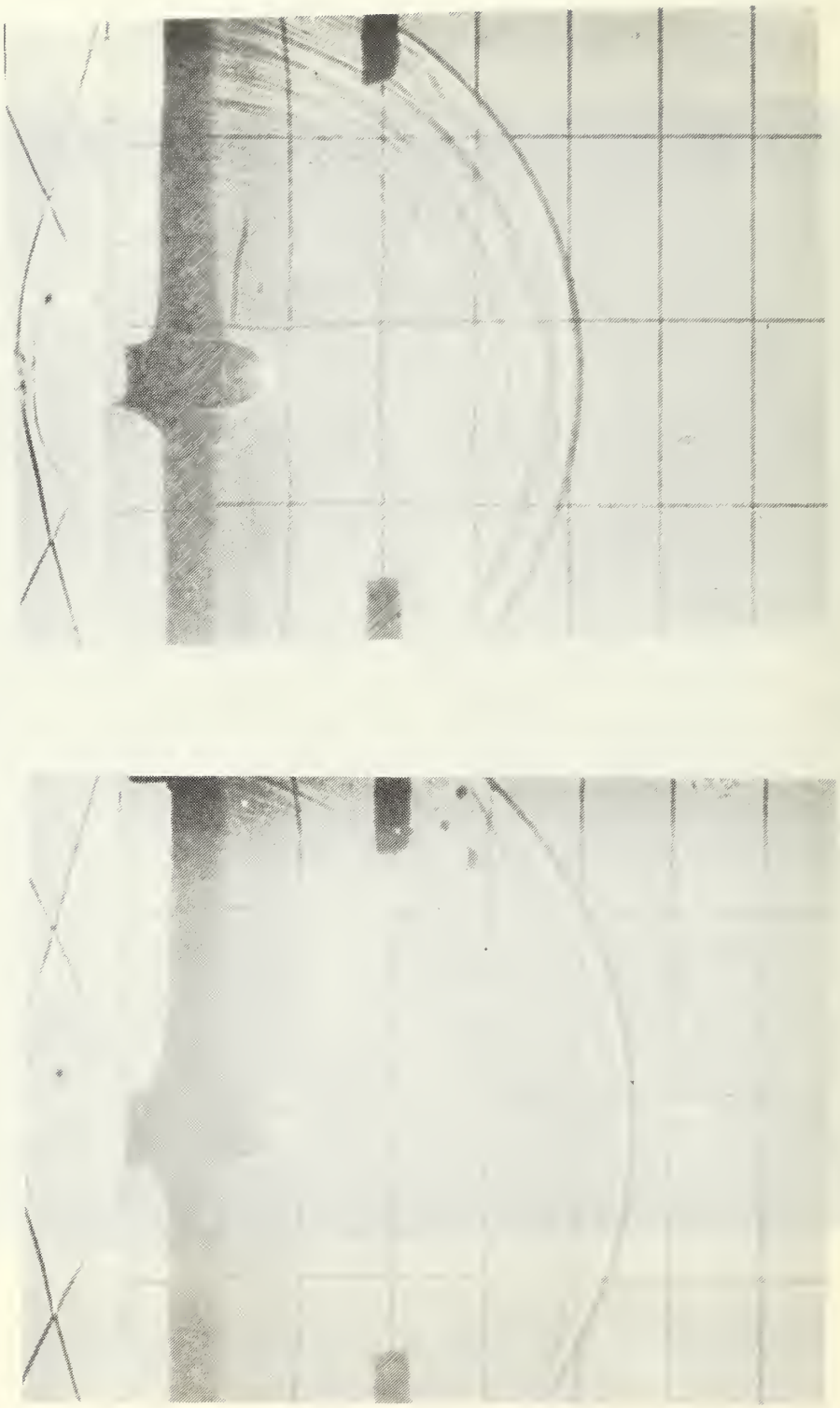

Figure IV-B-2: Shock Waves Resulting from a Prepunched Hole Impact

(This page intentionally blank)

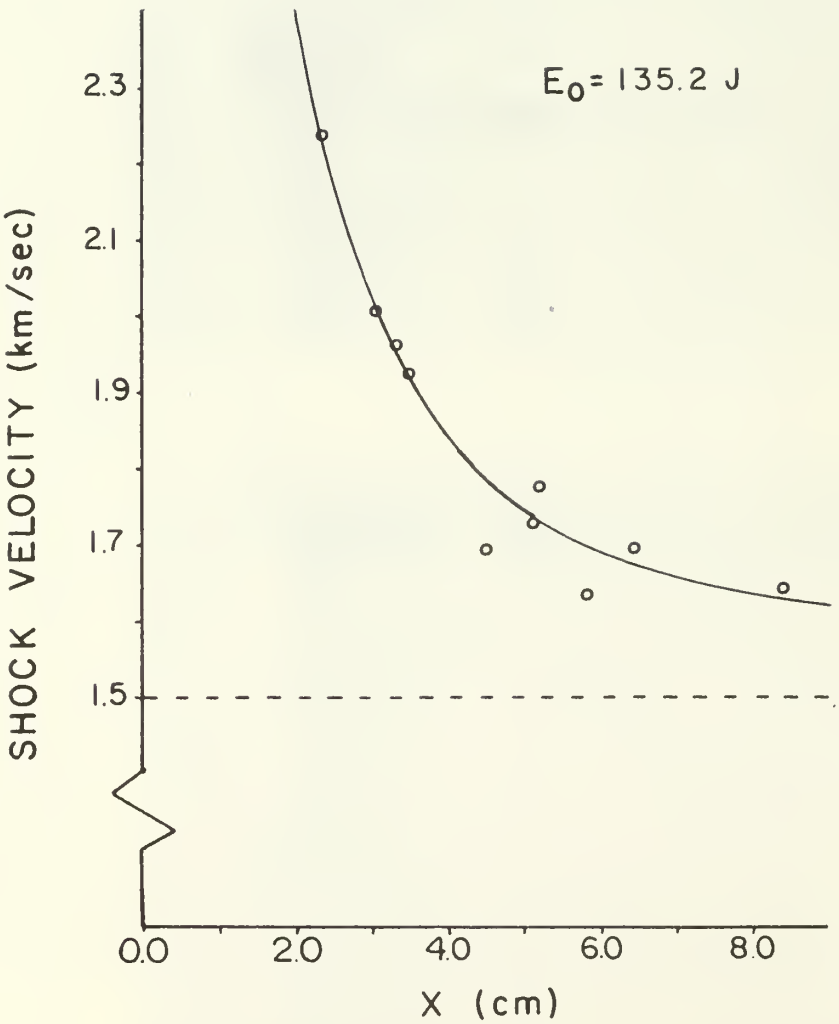


Figure IV-B-3 Shock Front Velocity Generated in Water by Projectile Impact.

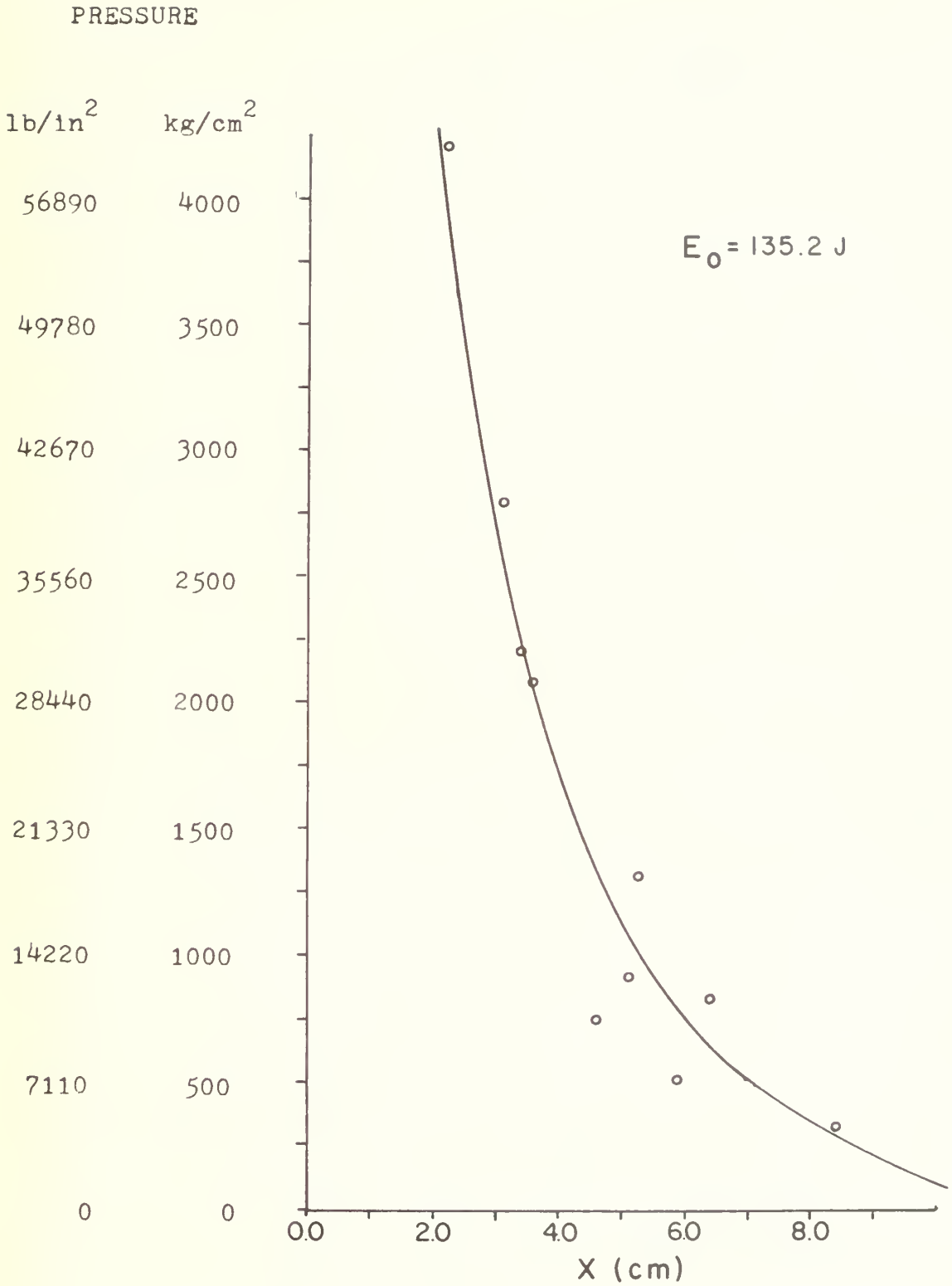


Figure IV-B-4 Shock Front Pressure Generated in Water by Projectile Impact.

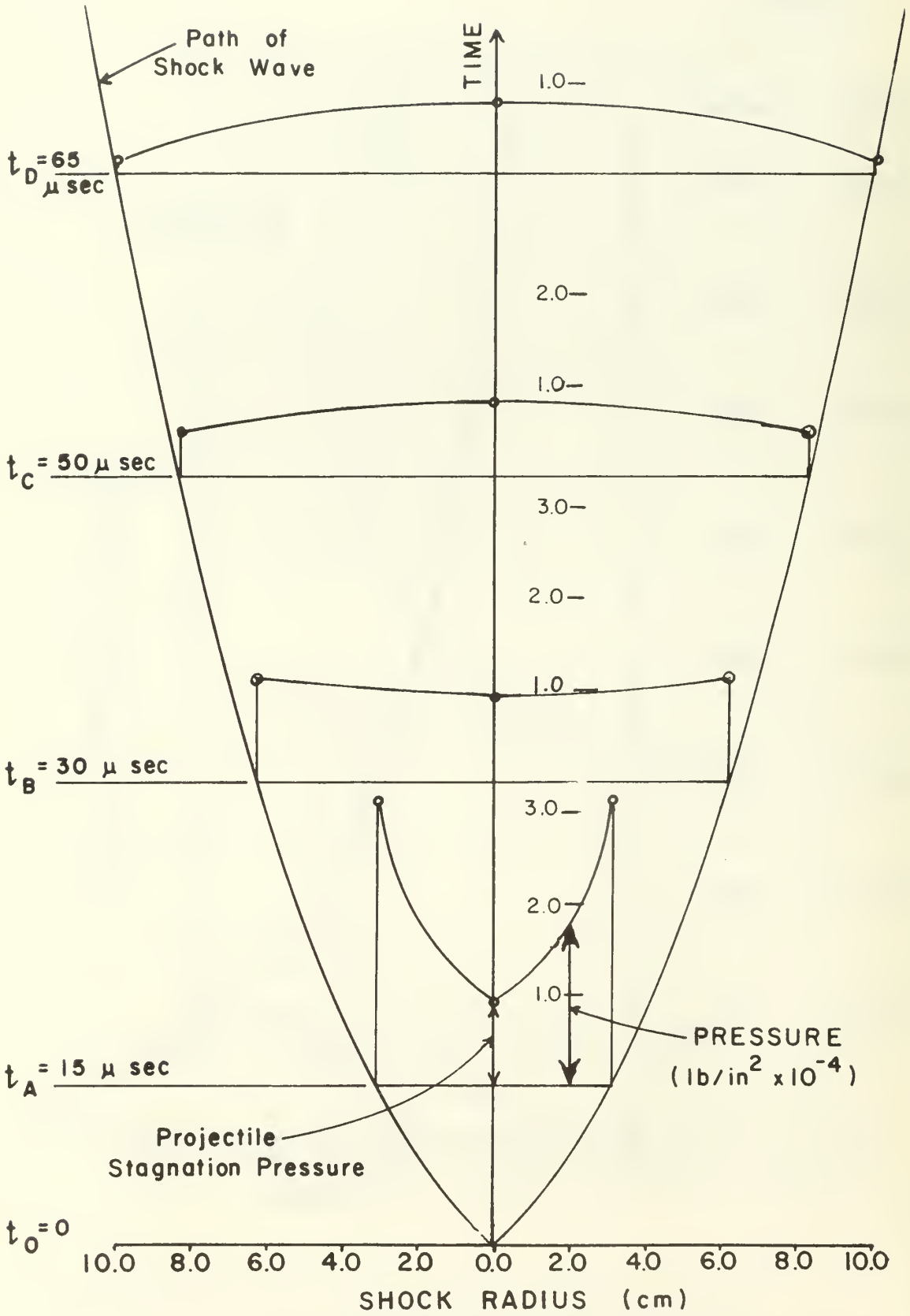


Figure IV-B-5 Evolution of Pressure in the Transition from Shock to Cavity Phase.

Figure IV-B-6: Cavity Growth Resulting from a Prepunched Hole Impact

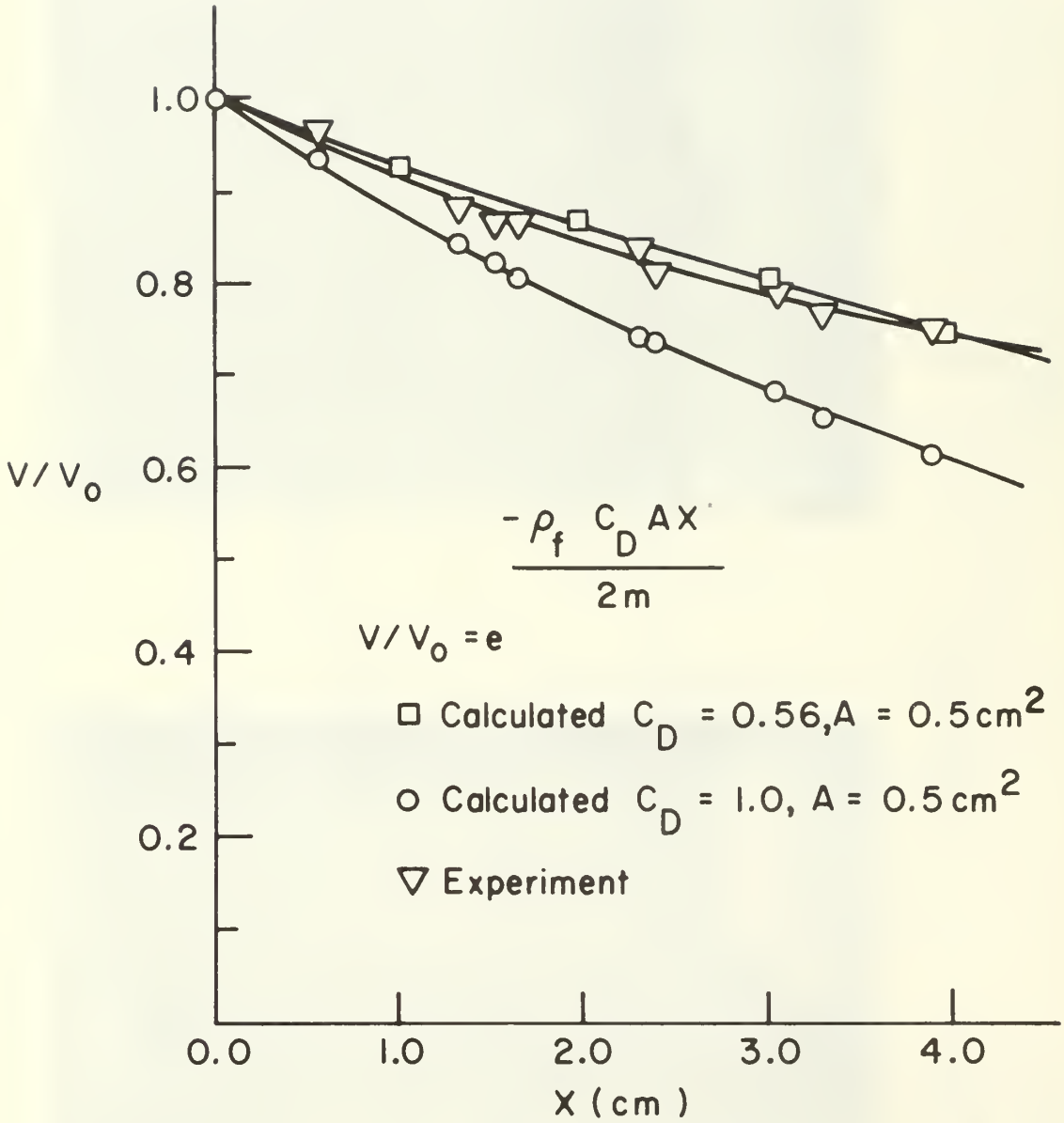


FIGURE IV-B-7 PROJECTILE VELOCITY DECAY RATIO AS A FUNCTION OF DISTANCE INTO TANK

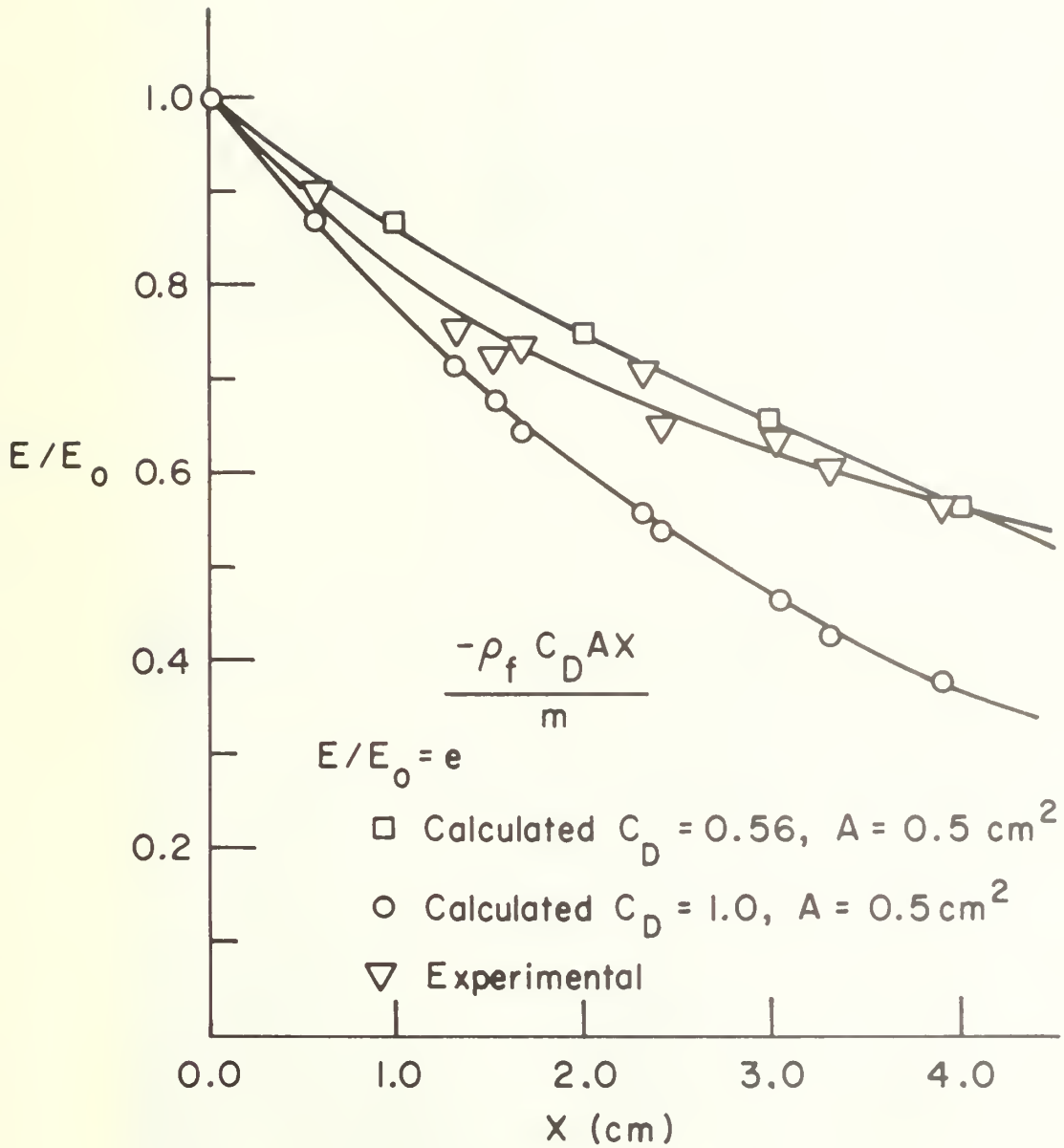


FIGURE IV-B-8 EXPERIMENTAL AND CALCULATED RATIOS OF PROJECTILE ENERGY

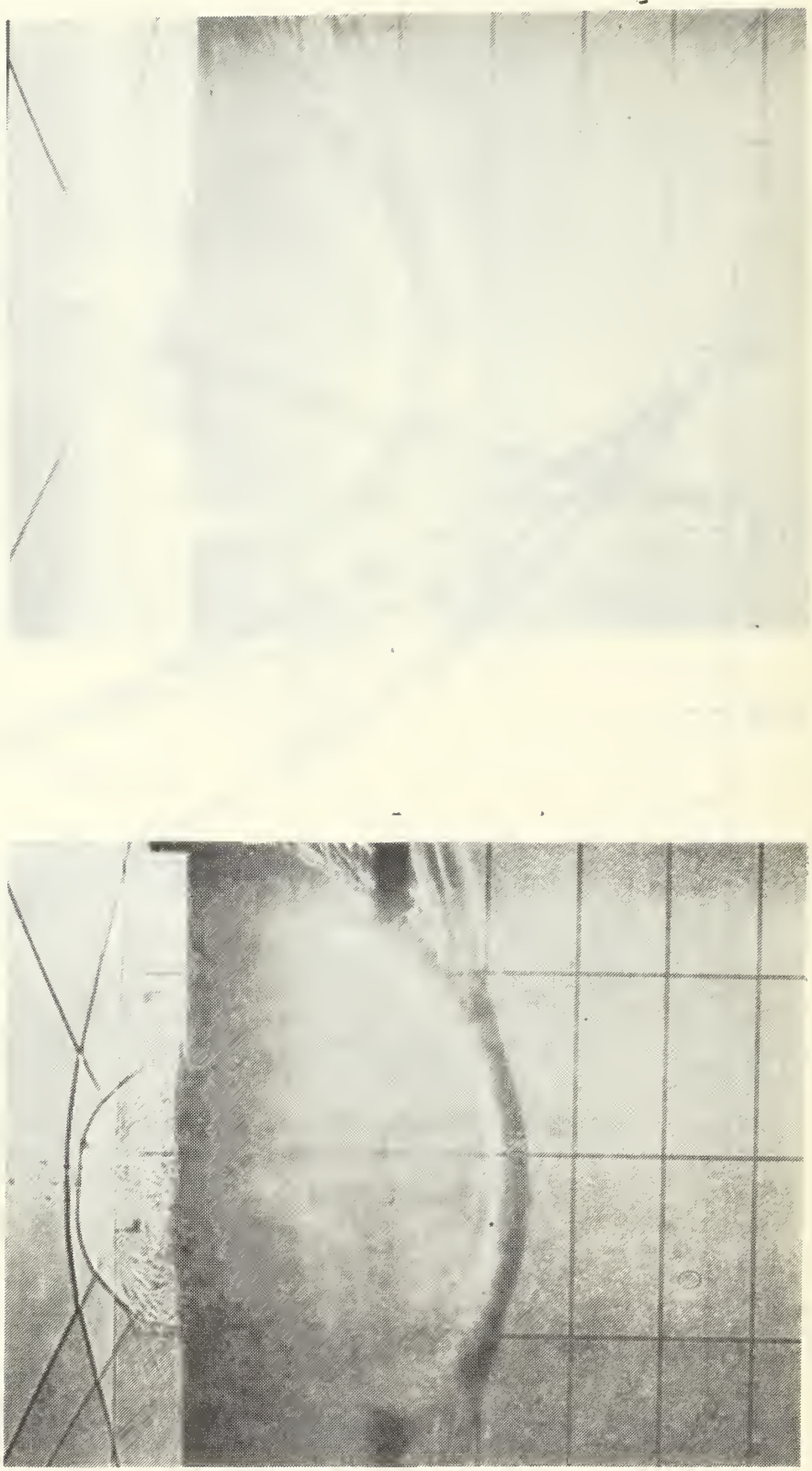

Figure IV-B-9 Shock Waves Resulting from 0.22 Caliber Camber Projectile Impact

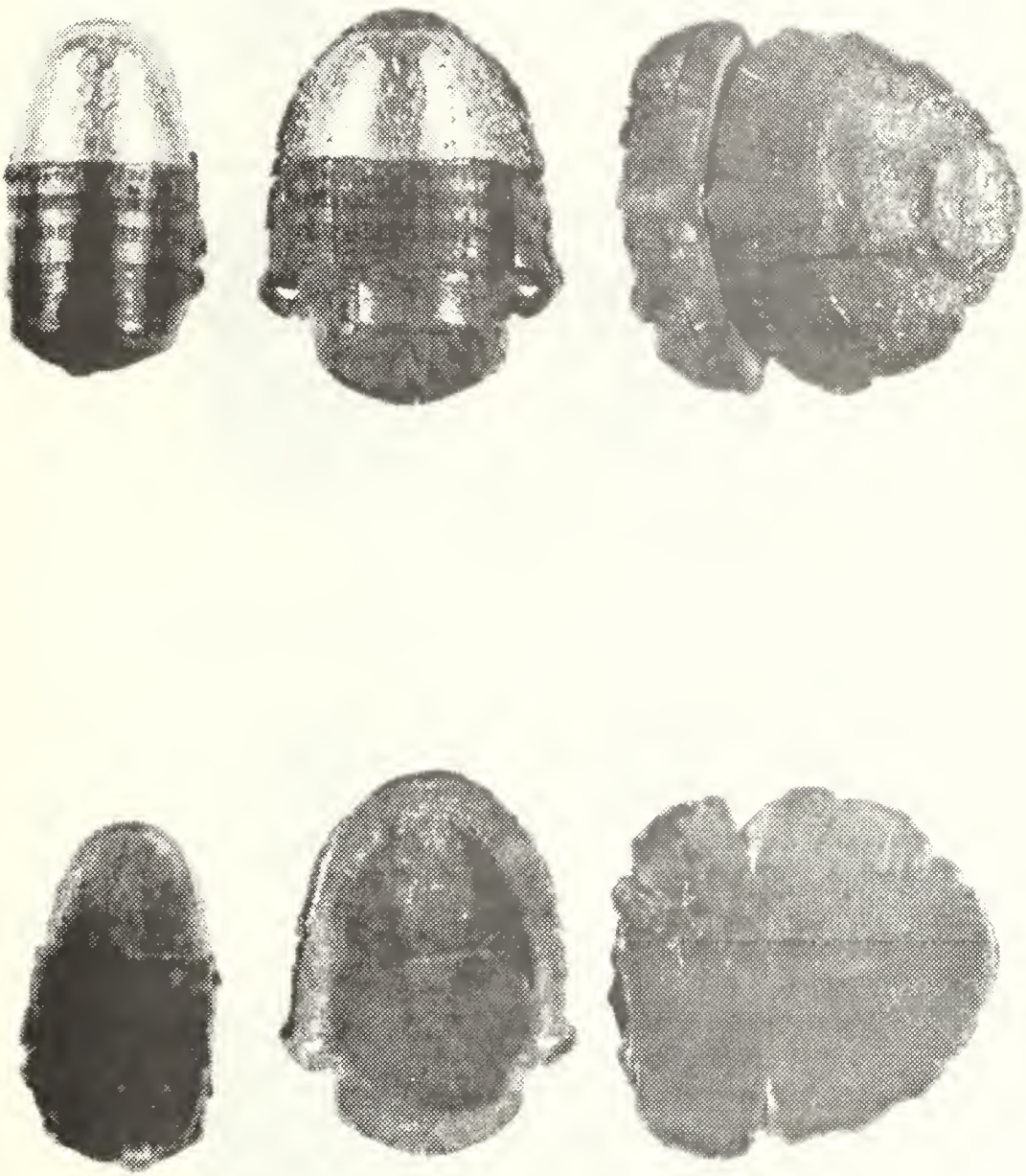

Figure IV-B-10 Projectiles After Impact Through Pre-punched Entry Wall

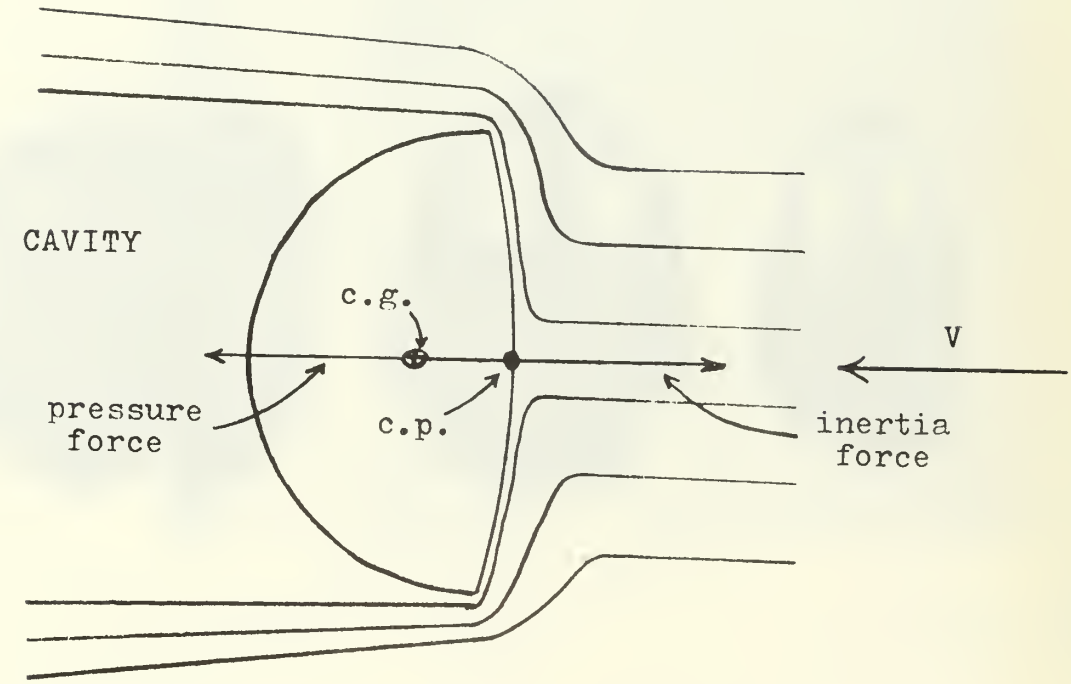


(A) At equilibrium

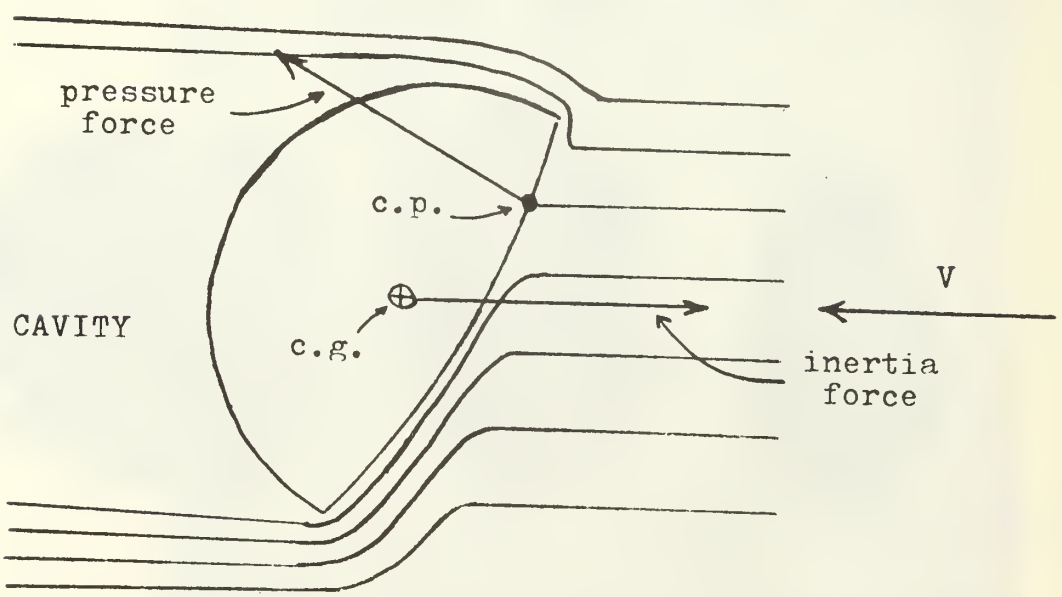


(B) Displaced from equilibrium

Figure IV-B-11 Dynamic Stability of a Deformed Projectile in Water After Impact.

Figure IV-B-12 Projectiles After Impact Through Solid Entry Wall.

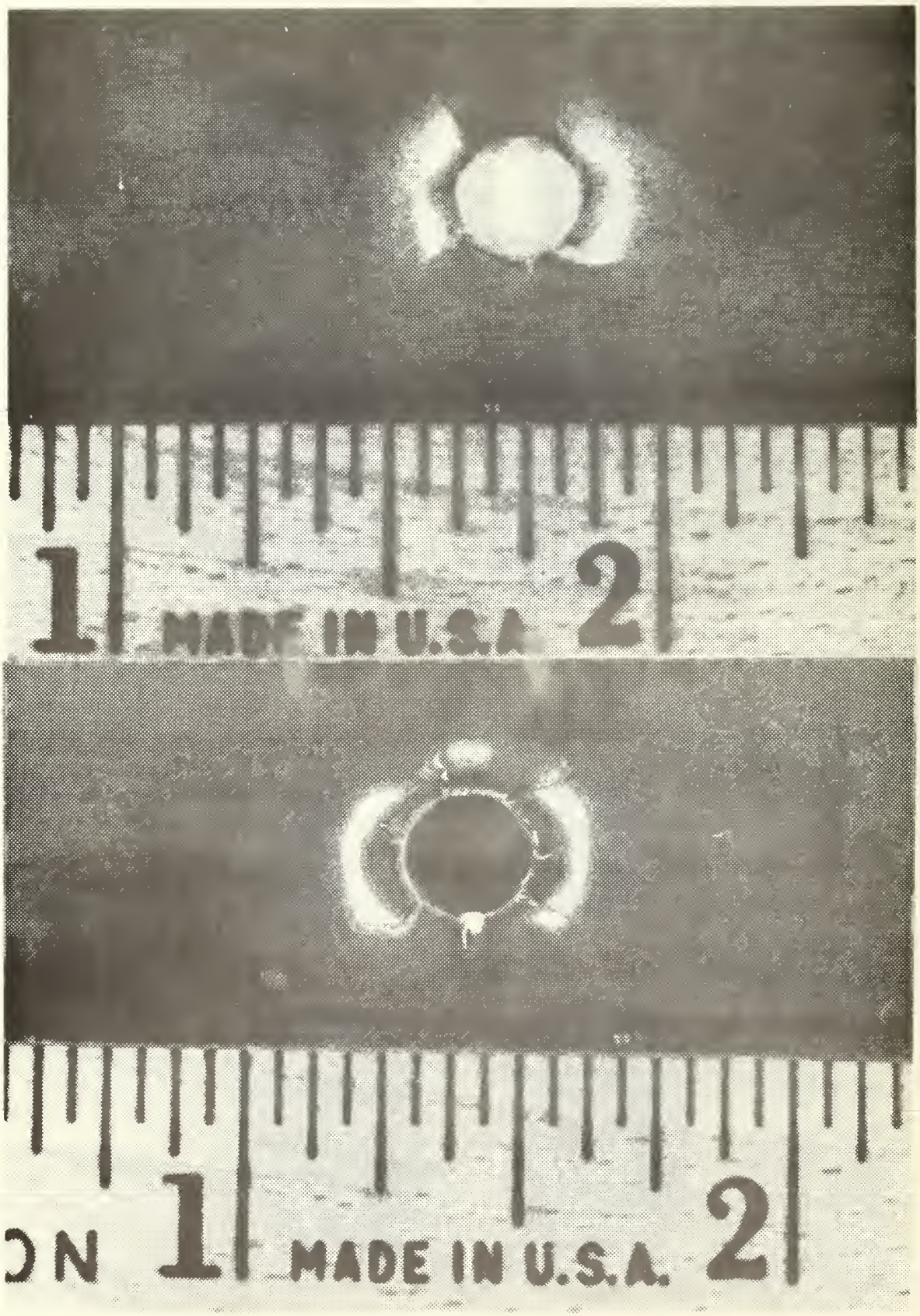


Figure IV-B-13 Solid Entry Wall After Impact

## V. RECOMMENDATIONS FOR FURTHER STUDY

In FY 74, Hydraulic Ram Studies will be continued in the Department of Aeronautics. The following items are recommended as an outline for this future work:

1. Shock phase shadowgraph studies should be extended to higher energy and caliber projectiles. Toward this end an experimental test tank capable of withstanding the damage caused by these projectiles has been designed. Information produced by the above studies should be correlated with analytical predictions of Yurkovitch.
2. The test tank should be instrumented to measure internal pressures during the shock and cavity phases. This data will allow assessment of the Yurkovitch predictions during shock phase and Lundstrom predictions during the cavity phase.
3. The test tank entry wall should be instrumented with strain gages to measure wall stresses during hydraulic ram. This data will allow assessment of structural interaction prediction methods.
4. The test tank entry wall should be instrumented to obtain wall motion during hydraulic ram. A fiber optic proximity gage is suggested as the measuring technique. This information will allow assessment of the structural interaction prediction method.
5. Continuing studies should be made to ascertain the validity of the combined piston theory - fluid pressure analytical-numerical approach and to improve the methods where ever possible.

## VI. REFERENCES CITED


1. Bedrosian, B. and DiMaggio, F. L., "Acoustic Approximations In Fluid-Shell Interactions," Journal of the Engineering Mechanics Division ASCE, Vol. 98, No. EM3, pp. 731-742, June 1972.

2. Klosner, J. M., "Inadequacies of Piston Theory In Fluid-Shell Interactions," Journal of the Engineering Mechanics Division ASCE, Vol. 96, No. EM2, pp. 143-159, April 1970.

3. Lundstrom, E. A., "Fluid Dynamic Analysis of Hydraulic Ram," NWC TP 5227, July 1971.

4. Yurkovitch, R. N. "Hydraulic Ram: A Fuel Tank Vulnerability Study," McDonnell Aircraft Engineering Methods Authorization, F65-76-555, September 1969.

5. Ball, R. E. "A Program for the Nonlinear Static and Dynamic Analysis of Arbitrarily Loaded Shells of Revolution," Computers and Structures, Vol. 2, pp. 141-162, 1972.

6. Ball, R. E. "A Computer Program for the Geometrically Nonlinear Static and Dynamic Analysis of Arbitrarily Loaded Shells of Revolution, Theory and Users Manual," NASA CR - 1987, 1972.

7. Holm, D. P., "Hydraulic Ram Shock Wave and Cavitation Effects on Aircraft Fuel Cell Survivability," MSAE Thesis, Naval Postgraduate School, Monterey, CA, September, 1973.

8. Bates, K. S., "Aircraft Fuel Tank Entry Wall-Projectile Interaction Studies," MSAE Thesis, Naval Postgraduate School, Monterey, CA, June 1973.

9. Formen, R. G., Parker, W. H., Sundirson, A. W., and Bitek, A., "Vulnerability of Aircraft Structures Exposed to Small Arms Fire Projectile Impact Damage," AFFDL TR 67-157, Feb. 1968.

10. Cole, R. H., "Underwater Explosions," Princeton University Press, 1948.

## VII LIST OF FIGURES


| Figure | | Page |
|---|---|---|
| II-A-1: | Idealization for a Single Degree of Freedom Analysis | 13 |
| II-A-2a: | Wall Pressure verses Time ($t < 1000$ $\mu$ sec) | 14 |
| II-A-2b: | Wall Pressure verses Time ($t < 100$ $\mu$ sec) | 15 |
| II-B-1: | Shock Pressure Distribution for .50 Caliber Projectile Impacting | 19 |
| II-B-2: | Normal Displacement verses Radial Distance Without Fluid Interaction | 20 |
| II-B-3: | Displacement of Fuel Tank Wall with Piston Theory | 21 |
| II-D-1: | Cavity Collapse Time from an Initial Radius of 0.5 Foot | 28 |
| II-D-2: | Cavity Collapse Time from an Initial Radius of 0.1 Foot | 29 |
| II-D-3: | Hydraulic Ram Cavity Pressure Oscillation | 30 |
| III-B-1: | Ballistic Range Components | 33 |
| III-B-2: | Ballistic Range Rifle Mounting System | 34 |
| III-B-3: | Ballistic Range Rifle Mount | 35 |
| III-B-4: | Ballistic Range Shadowgraph Station | 36 |
| III-B-5: | Delayed Pulse Generator Circuitry | 37 |
| III-B-6: | Shadowgraph of a 63 gr. Semi-Point with a Velocity of 2941 fps | 38 |
| III-B-7: | Shadowgraph of a 50 gr. Spitzer Used in Range Calibration with a Velocity of 3080 fps | 38 |
| III-B-8: | Ballistic Range Configuration (Down Range View) | 39 |
| III-B-9: | Ballistic Range Configuration (Up Range View) | 40 |
| III-B-10: | Ballistic Range Bullet Catcher | 41 |
| III-C-1: | Test Specimen Setup | 43 |
| III-C-2: | Fuel Tank Test Setup | 44 |
| III-C-3: | Test Tank and Stand | 45 |

| Figure | | Page |
|---|---|---|
| IV-A-1: | Flow Field After Plate Penetration | 49 |
| IV-A-2: | Exit Velocity verses Impact Velocity for Two 22.2 Caliber Projectile Shapes Fired Normal to a 0.99 Inch Thick 7075-T6 Aluminum Plate | 50 |
| IV-A-3: | Exit Velocity verses Impact Velocity for a 55 gr Semi-Pointed 22.2 Caliber Projectile Fired Normal to a .09 inch thick 7075-T6 Aluminum Plate. | 51 |
| IV-A-4: | Exit Velocity verses Impact Velocity for a 63 gr Semi-Pointed 22.2 Caliber Projectile Fired Normal to a .09 inch thick 7075-T6 Aluminum Plate. | 52 |
| IV-A-5: | Kinetic Energy Loss Verses Initial Velocity for a Range of Projectile Masses and Shapes. | 53 |
| IV-B-1: | Test Tank After Impact of 22.2 Caliber High Energy Projectile. | 60 |
| IV-B-2: | Shock Waves Resulting from a Prepunched Hole Impact | 61 |
| IV-B-3: | Shock Front Velocity Generated in Water by Projectile Impact | 63 |
| IV-B-4: | Shock Front Pressure Generated in Water by Projectile Impact | 64 |
| IV-B-5: | Evolution of Pressure in the Transition from Shock to Cavity Phase | 65 |
| IV-B-6: | Cavity Growth Resulting from a Prepunched Hole Impact | 66 |
| IV-B-7 | Projectile Velocity Decay Ratio as a Function of Distance into Tank | 67 |
| IV-B-8 | Experimental and Calculated Ratios of Projectile Energy | 68 |
| IV-B-9: | Shock Waves Resulting from a .22 Caliber Projectile Impact | 69 |
| IV-B-10: | Projectile After Impact through Prepunched Entry Wall | 70 |
| IV-B-11: | Dynamic Stability of a Deformed Projectile in Water After Impact | 71 |
| IV-B-12: | Projectile After Impact through Solid Entry Wall | 72 |
| IV-B-13: | Solid Entry Wall After Impact | 73 |

## DISTRIBUTION LIST

| | | No. of Copies |
|---|---|---|
| 1. | Library<br>Code 0212<br>Naval Postgraduate School<br>Monterey, California 93940 | 2 |
| 2. | Department of Aeronautics<br>Code 57<br>Naval Postgraduate School<br>Monterey, California 93940 | 13 |
| | Prof. R. W. Bell, Chairman | 1 |
| | Prof. R. E. Ball | 2 |
| | Prof. A. E. Fuhs | 5 |
| | Prof. H. L. Power | 5 |
| 3. | Prof. J. M. Wozencraft<br>Code 023<br>Dean of Research Administration<br>Naval Postgraduate School<br>Monterey, California 93940 | 1 |
| 4. | Defense Documentation Center<br>Cameron Station<br>Alexandria, Virginia 22314 | 12 |
| 5. | Dr. Eric Lundstrom<br>Naval Weapons Center<br>China Lake, California | 2 |
| 6. | Capt. Phillip Fry<br>Air Force Flight Dynamics Laboratory<br>Dayton, Ohio | 2 |
| 7. | CDR M. L. Johnson<br>USN (AIR-09JA)<br>Naval Air Systems Command<br>Washington, D.C. 20361 | 1 |
| 8. | Capt James McNerney<br>DDR&E<br>Pentagon<br>Washington, D.C. 20370 | 1 |